Novel Techniques for Improving the Accuracy of 3D3C Optical Velocimetry

A

Dissertation

Presented to

the faculty of the School of Engineering and Applied Science

University of Virginia

in partial fulfillment

of the requirements for the degree

Doctor of Philosophy

in Mechanical and Aerospace Engineering

by

Ning Liu

August 2020

APPROVAL SHEET

This

Dissertation

is submitted in partial fulfillment of the requirements
for the degree of

Doctor of Philosophy

Author: Ning Liu

This Dissertation has been read and approved by the examing committee:

Advisor: Lin Ma

Advisor:

Committee Member: Daniel B. Quinn

Committee Member: Patrick E. Hopkins

Committee Member: Zongli Lin

Committee Member: Xiaodong Li

Committee Member:

Committee Member:

Accepted for the School of Engineering and Applied Science:

Craig H. Benson, School of Engineering and Applied Science

August 2020

Abstract

3D3C (three-dimensional and three-component) optical velocimetry has long been desired to resolve the 3D spatial structures of turbulent flows. Recent advancements have demonstrated tomographic particle image velocimetry (tomo-PIV) as a powerful technique to enable such velocimetry. The current tomo-PIV technique obtains 3D3C velocimetry by combining PIV measurements with 3D tomographic reconstruction, i.e., cross-correlating the 3D particles distributions reconstructed by tomography at two consecutive times. However, the current tomo-PIV technique, due to the significant complexity of tomography (e.g., the view registration VR process and the reconstruction algorithm), suffers from the relatively low accuracy of velocity measurements. This further deteriorates the subsequent determinations of velocity derivatives which are usually of ultimate interests. To study and address such accuracy issue, this dissertation first reports an experimental quantification of the tomo-PIV accuracy, and then reports the developments and demonstrations of two novel techniques to enhance the tomo-PIV accuracy.

First, the accuracy of the existing tomo-PIV technique was quantified experimentally. Precisely controlled experiments were designed using tracer particles embedded in a solid sample, and tomo-PIV measurements were performed on the sample while it was moved both translationally and rotationally to simulate various known displacement fields. So that the 3D3C displacements measured by tomo-PIV can be directly compared to the known displacements created by the sample to quantify the accuracy. With these controlled

experiments, the accuracies in both velocity magnitude and direction were quantified and analyzed in this dissertation.

Then, after recognizing the current tomo-PIV accuracy, two techniques were proposed in this dissertation to significantly enhance the accuracy of tomo-PIV measurements. These two techniques were code-named the RTPIV (regularized tomo-PIV) method and the RIVR (reconstruction integrating view registration) method. Conceptually, the RTPIV method improved the accuracy of 3D3C velocity measurements by incorporating the conservation of mass (COM) equation as *a priori* information into the cross-correlation. The RIVR method enhanced the accuracies of tomography and the resulting velocity by integrating the tomography and VR. The accuracy enhancement could be achieved, because the integration of tomography and VR established a feedback mechanism between them and enabled each step to leverage the information provided by the other. Both the RTPIV and RIVR methods were validated experimentally and numerically, and were demonstrated to indeed enhance the accuracy of tomo-PIV measurements significantly. The measurements with enhanced accuracy by these two techniques are expected to improve the understanding of flow and combustion physics and the design of propulsion systems.

Acknowledgement

First and foremost, I would express my sincere thanks and deepest gratitude to my advisor, Prof. Lin Ma, for providing me with insightful guidance, valuable inspiration and unyielding support. Prof. Ma has taught me how to effectively and efficiently perform research, and especially provided great help on my scientific writing and communication. Beyond the research, at a philosophy level, he has also taught me how to establish principles and apply principles to daily life.

I would appreciate Prof. Daniel Quinn, Prof. Patrick Hopkins, Prof. Zongli Lin, and Prof. Xiaodong Li for serving on my advisory committee and providing academic and professional suggestions.

I would also thank my lab mates at both University of Virginia and Virginia Tech for accompanying me on such unforgettable and rewarding journey. They are Dr. Fan He, Dr. Yue Wu, Dr. Qingchun Lei, Dr. Wenjiang Xu, Dr. Haoting Wang, Dr. Yihua Ren, Mr. Ke Zhou, Ms. Qian Wang, Mr. Chris Windle, and many others.

I would like to acknowledge the financial support from the National Science Foundation (Award Number: 1803470 and 1839603), which makes this work possible.

Last but not least, my greatest thanks go to my parents and other family members for their love, understanding, and encouragement.

Table of Contents

List of Figures

Chapter 1 Introduction

1.1 Overview of 3D3C particle image velocimetry

Particle image velocimetry (PIV) is a well-established technique for two-dimensional and two-component (2D2C) velocity measurements in the study of fluid flows [1, 2]. Practical applications ubiquitously involve three-dimensional (3D) flows containing 3D structures (e.g., vortices, and shear layer, etc.), and the ability to measure the three-dimensional and three-component (3D3C) velocity field has been highly desired. Several possible approaches have been investigated to extend the established 2D2C PIV technique to 3D3C measurements by leveraging techniques from other disciplines, including scanning PIV [3-5], holographic PIV [6, 7], and tomographic PIV (tomo-PIV) [8-11]. Different 3D3C PIV techniques have different working principles. Among aforementioned techniques, scanning PIV is a conceptually straightforward approach which obtains a 3D3C velocity measurement by a series of 2D3C measurements sequentially using the established stereoscopic PIV technique. However, its spatial resolution in the scanning direction has been typically limited to the order of ~1 mm [4, 12, 13], due to practical difficulties related to precise control of the scanning, laser repetition rate, and camera frame rate. Holographic PIV also offers great promise for 3D3C velocity measurements. This technique obtains the 3D3C velocity by combining holography with PIV, more specifically by encoding the amplitude and phase of the scattered light, then reconstructing and cross-correlating the particle distribution. However, at this stage of its development, practical applications are limited by the time-consuming reinstallation process of hologram films [14-16]. Similar to scanning PIV, tomo-PIV is an extension of the established 2D PIV measurements, and it obtains 3D3C velocity measurements by combining PIV measurements with 3D tomographic reconstruction, more specifically by cross-correlating two 3D particle distributions reconstructed using two sets of particle projections captured by multiple cameras at two consecutive times. Compared to the scanning PIV technique, the tomo-PIV technique enables instantaneous measurement without scanning, and enables spatial resolution down to ~0.10 mm in all three spatial directions [2]. Compared to the holographic techniques, the tomo-PIV technique takes advantages of recent advancements in high-repetition-rate CCD and CMOS cameras, and enables an all-digital data acquisition and processing implementation. Due these advantages, tomo-PIV has been studied and applied under a range of application backgrounds and in both passive and reactive flows [9, 17, 18]. And this dissertation focuses on the tomo-PIV technique.

1.2 Tomographic PIV

Typically, the tomo-PIV technique involves two steps: tomography reconstruction and cross-correlation. In the first step, the tomography reconstruction step, the distributions of seeded particles in 3D are obtained at two consecutive times using 3D tomographic reconstructions. At each time, a thick laser slab is used to illuminate the seeded particles volumetrically, and multiple cameras are used to capture the scattered signal from different orientations, providing the inputs for a tomography algorithm to obtain the 3D distribution of the seeded particles. In the second step, the cross-correlation step, a 3D3C velocity field is calculated by performing a cross-correlation of the two frames of 3D particle distributions obtained in the first step.

However, the tomo-PIV technique, due to its significant complexity of tomography (the aforementioned step 1), suffers from the relatively low accuracy, compared to 2D PIV measurements. For instance, due to the nature of the volumetric illumination and the use of multiple cameras, it becomes important to calibrate these cameras both in terms of their noise level and their relative orientation, which is the so-called view registration (VR) process. Such calibration inevitably involves uncertainties, including camera noise and also orientation error [19], and these uncertainties propagate through the rest of the data processing for obtaining velocity. Also, the subsequent tomography algorithm can only reconstruct with a finite accuracy even if the measurements captured by the cameras are error free. In practice, these measurements are contaminated by noises (e.g., due to the calibrations just mentioned), and such noises will propagate during the tomographic reconstruction process. As a result, accuracy of tomo-PIV can be much worse than that of 2D PIV. Currently, the measurement accuracy of 3D3C velocity enabled by tomo-PIV was reported to be on the order of ~1 voxel and ~2° in terms of velocity magnitude and direction [19], respectively; in contrast, the 2D PIV technique can yield a measurement accuracy of ~0.5 pixel and ~1° [20, 21].

Furthermore, the existing error of velocity measurements propagates or becomes amplified when inferring velocity derivatives, including velocity-gradient-type derivatives (e.g., stress and vortex) and velocity-integral-type derivatives (e.g., force and energy). These derivatives are of paramount importance to the understanding of aerodynamics and the design of propulsion systems. Based on our quantifications, the aforementioned error of ~1 voxel and ~2° in velocity magnitude and direction would lead to at least ~35% error in the determination of the velocity-gradient-type derivatives (e.g., stress and vorticity), and also lead to at least ~20% error in the determination of velocity-integral-type derivatives (e.g., force and energy). These error levels are high enough to change or even completely reshape our understanding of flow physics (e.g., flow topology and vortex dynamics) and the design of propulsion systems (e.g., geometric parameters and fuel consumption of aero-engines).

Recognizing the additional complexity brought about by tomo-PIV and the critical need for accuracy, considerable efforts have been made to enhance the measurement accuracy of tomo-PIV from tomography reconstruction (step 1) and cross-correlation (step 2). The investigation of tomography reconstruction included a range of experimental and computational efforts to improve the reconstruction accuracy. Experimental effects included the optimization of key imaging parameters [19, 22, 23], tomography imaging configuration (cross-like configuration [24, 25] and linear configuration [26, 27]), view registration [28-30], seeding density [31, 32], etc. In parallel, computational efforts included optimization of existing reconstruction algorithms such as ART (algebraic reconstruction technique) and MART (multiplicative algebraic reconstruction technique) [8, 33], the use of spatial filter in the reconstruction [33], the integration of sparsity maximization into reconstruction [34, 35], and the development of new reconstruction methods and algorithms [29, 36, 37], etc. In addition to the investigation in tomography reconstruction, significant efforts have also been invested in the improvement of the second step, the cross-correlation step. Examples include the development of high-accuracy cross-correlation algorithms such as the 3D window deformation algorithm [38], methods for sub-voxel estimation [5], and the use of low-pass filters in 3D image pre-processing [39].

1.3 Organization and contributions of this dissertation

Based on the above understanding of past efforts, this dissertation is aimed to study and address the accuracy issue in tomo-PIV measurements. This dissertation first reports an experimental quantification of the current tomo-PIV accuracy, and then reports two novel techniques to improve the accuracy, as organized below, together with the main contributions. More specifically:

Chapter 2 introduces a quantification of tomo-PIV accuracy using controlled experiment measurements [19], and sets the ground work for the following work in Chapter 3 and 4. The main contribution of this part is that we, for the first time, experimentally quantified the tomo-PIV accuracy by precisely controlled measurements. The controlled measurements were designed by performing tomo-PIV measurements on a solid sample embedded with tracer particles, while the sample was moved both translationally and rotationally to create various known displacement fields. So that the 3D3C displacements measured by tomo-PIV can be directly compared to the known displacements created by the sample. The results illustrated that the tomo-PIV technique was able to reconstruct the 3D3C velocity with an averaged error of 0.8–1.4 voxels in terms of magnitude and 1.7°–1.9° in terms of orientation for the velocity fields tested. These results obtained from controlled tests are expected to aid the error analysis and the developments of advanced tomo-PIV techniques.

After recognizing the current tomo-PIV accuracy, Chapter 3 and 4 then present two advanced techniques to significantly enhance the accuracy of the tomo-PIV measurements. These two techniques are code-named the RTPIV (regularized tomo-PIV) method [40] and the RIVR (reconstruction integrating view registration) method [29, 30].

Chapter 3 describes the development and the validation of the RTPIV method, motivated by the need of tomo-PIV accuracy enhancement. The main contribution is the development of the RTPIV method, a regularized method that can be applied to incompressible flows and other types of flows where the density variation is negligible. The major idea of the RTPIV method is that it improves the accuracy of 3D3C velocity measurements by incorporating the conservation of mass (COM) equation as *a priori* information into the cross-correlation process. This RTPIV method was demonstrated and validated both experimentally and numerically. The results illustrated that the method was able to significantly enhance the accuracy of 3D3C velocity measurements, compared to the existing tomo-PIV technique.

Chapter 4 then describes the development and the validation of the RIVR method, also motivated by the requirement of accuracy improvement of 3D tomography diagnostics. The main contribution is the development and validation of the RIVR method. This method focuses on the tomography process, and it enhances the accuracies of tomography and the resulting velocity by integrating tomography and VR holistically. The accuracy enhancement can be achieved, because the integration of tomography and VR establishes a feedback mechanism between them and enables each step to leverage the information provided by the other. Both controlled experiments and accompanying numerical analyses were conducted to validate the RIVR method. Two sets of controlled experiments were conducted and analyzed, including a static uniform dye solution and turbulent flows, where the RIVR technique was demonstrated to significantly reduce the overall reconstruction error, compared to past methods that treated VR and tomography separately.

Lastly, Chapter 5 summarizes this dissertation and suggests the possible future work.

To summarize, the major contributions of this dissertation are:

1) The accuracy of 3D3C velocity measurements enabled by the tomo-PIV technique was experimentally quantified for the first time by designing precisely controlled experiments on a solid sample embedded with tracer particles.

2) The RTPIV method was developed and demonstrated to considerably enhance the accuracy of 3D3C velocity measurements. This RTPIV method is applicable to measurements in incompressible flows or other types of flows where the density variation is negligible.

3) The RIVR method was developed and demonstrated to significantly improve the accuracy of 3D tomography diagnostics including tomo-PIV. This RIVR method is applicable universally to various types of 3D tomography diagnostics, not only limited to tomo-PIV, but also including tomographic laser induced fluorescence and tomographic chemiluminescence, etc.

Chapter 2 Experimental quantifications of tomo-PIV uncertainty

Abstract

The goal of this work was to experimentally quantify the uncertainty of three-dimensional (3D) and three-component (3C) velocity measurements using tomographic particle image velocimetry (tomo-PIV). Controlled measurements were designed using tracer particles embedded in a solid sample, and tomo-PIV measurements were performed on the sample while it was moved both translationally and rotationally to simulate various known displacement fields. So that the 3D3C displacements measured by tomo-PIV can be directly compared to the known displacements created by the sample. The results illustrated that 1) the tomo-PIV technique was able to reconstruct the 3D3C velocity with an averaged error of 0.8 to 1.4 voxels in terms of magnitude and 1.7° to 1.9° in terms of orientation for the velocity fields tested, 2) view registration (VR) plays a significant role in tomo-PIV, and by reducing VR error from 0.6° to 0.1°, the 3D3C measurement accuracy can be improved by at least 2.5× in terms of both magnitude and orientation, and 3) the use of additional cameras in tomo-PIV can extend the 3D3C velocity measurement to a larger volume while maintaining acceptable accuracy. These results obtained from controlled tests are expected to aid the error analysis and the design of tomo-PIV measurements.

2.1 Introduction

Particle image velocimetry (PIV) is a well-established technique for two-component (2C) velocity in two-dimension (2D) [1, 2]. Practical applications ubiquitously involved

3D flows, and the ability to measurement 3D3C velocity fields is highly desired. Several possible approaches have been investigated to extend the established 2D2C PIV technique to 3D3C measurements, including scanning PIV [3-5], holographic PIV [6, 7], and tomographic PIV (tomo-PIV) [8-11]. Among these techniques, scanning PIV is a conceptually straightforward approach which obtains a 3D velocity measurement by a series of 2D measurements sequentially using the established 2D PIV technique. However, its spatial resolution in the scanning direction has been typically limited to the order of ~1mm [4, 12, 13] due to practical difficulties related to precise control of the scanning, laser repetition rate, and camera frame rate. Holographic PIV also offers great promise for 3D3C velocity measurements. However, at this stage of its development, practical applications are limited by the time consuming reinstallation process of hologram films [14-16]. Similar to scanning PIV, tomo-PIV obtains 3D3C velocity measurements by extending the established 2D PIV measurements [8-10]. The technique uses a thick laser slab to illuminate the seeded particles volumetrically, and uses multiple cameras to image the scattered signal from multiple orientations, based on which a tomographic reconstruction was performed to obtain the particle position distributions in 3D. Compared to the scanning PIV technique, the tomo-PIV technique enables instantaneous measurement without scanning, and enables spatial resolution down to ~0.10 mm in all three spatial directions [2]. Compared to holographic techniques, the tomo-PIV technique takes advantages of recent advancements in high-repetition-rate CCD and CMOS cameras, and enables an all-digital data acquisition and processing implementation. Due these advantages, tomo-PIV has been studied and applied under a range of application backgrounds and in both passive and reactive flows [9, 17, 18].

Due to the promise and progress demonstrated in tomo-PIV, both numerical and experimental research efforts have been devoted to quantify its capability and accuracy. Numerical efforts included the use of simulations to validate and quantify the accuracy of tomo-PIV in canonical turbulent flows such as channel flows [41] and cylinder wake flows [8]. In parallel to these numerical efforts, experimental efforts have also been invested to validate and characterize the reconstruction quality of tomo-PIV [42] using flow measurements. These results provide insights into important factors such as SNR, intensity variance, and the relative quality factor. However, the use flows cannot provide the degree of control desired for error quantification. Therefore, it is desirable to have results that can provide direct experimental validation and quantification of tomo-PIV measurements, ideally from precisely controlled velocity fields.

Based on the above understanding of past efforts, this work reports an experimental validation of tomo-PIV by performing precisely controlled experiment. The experiment was performed using a custom-built cell with tracer particles seeded and fixed on a solid sample. A moving stage was installed under the cell and was able to precisely control the movement of the cell. Therefore, the particle displacement field between subsequent cell locations can be created to simulate various velocity fields with great precision. Then tomo-PIV measurement was performed and corresponding reconstructions were obtained, which were then compared with the exact velocity field to quantify the accuracy of the 3D3C measurements.

The rest of this chapter is organized as follows. Chapter 2.2 describes the controlled experimental setup used to validate the tomo-PIV technique. Chapter 2.3 reports the validation results together with the accompanying analysis. Finally, Chapter 2.4 summarizes the chapter.

2.2 Experimental arrangement

The experimental setup of the controlled measurement is schematically illustrated from the top view as shown in Figure 2-1. As shown in the center portion of Figure 2-1, the controlled cell consists of three components: a moving base, thin glasses and a clamp. The moving base was assembled by mounting a rotation stage (Thorlabs PR01) on a translation stage (OptoSigma TSD-602C). The translation stage can linearly translate along one direction with a resolution of 10 μm and the rotation stage can rotate continuously within 360^{o} with a resolution of 5 arcmin. Four pieces of thin glasses were fixed on the breadboard by using a clamp. The surfaces of glasses were adjusted parallel to each other and perpendicular to the breadboard plane. The spacing between two adjacent glasses is 5 mm. All glasses have a thickness of 0.50 mm and a height × width of 65 × 60 mm^2, and they were coated with 4.05 μm polystyrene particles on one side. Before coating, the particles were stored in a solution with a concentration of 10^{-7} solids by weight, and ultra-sonication was applied to prevent bead aggregation. Based on the controlled cell configuration, a Cartesian coordinate system was defined such that the plane of the breadboard was the *x*-*y* plane with the origin at plate center, as shown in Figure 2-1. The *x*, *y* and *z* axes were defined along the thickness, width and height direction of the glasses, respectively.

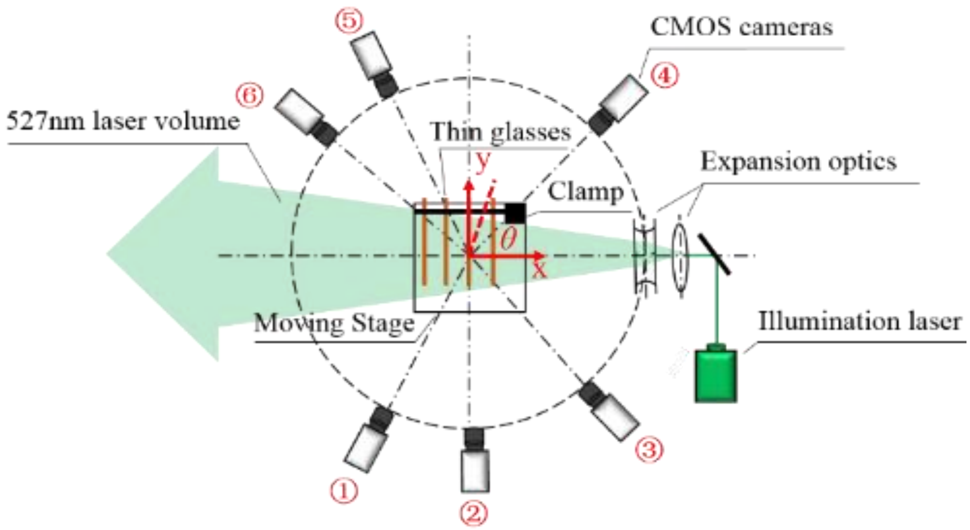

Figure 2-1 Experimental setup.

The output of a high pulse energy Nd: YLF laser (Photonics Industries DM30 – 527, labeled as Illumination laser in Figure 2-1 with a wavelength of 527 nm was used to illuminate the polystyrene particles on glass surfaces. Operated at a repetition rate of 1 kHz, the illumination laser generates pulses with a pulse energy of 50 mJ and a pulse duration of ~120 ns. The laser pulses were expanded by a series of lenses into a thick laser slab so that a measurement volume of 57 (*x* direction) × 57 (*y* direction) × 19 (*z* direction) mm^3 was illuminated. Note that typical tomo-PIV practice (e.g., the arrangement used in [1]) involves arranging the smallest dimension of the measurement volume normal to the plane formed by the optical axes of the cameras (assuming the cameras are arranged in a co-planar fashion). Such practice offers the advantage of minimizing particle overlapping on the projections at the cost of measurement volume. This work used a different arrangement to test if using more cameras (six compared to the typical practice of 4) can help to combat the overlapping effects and obtain measurements in a thicker volume (and the results suggested it can as to be elaborated in Section 3).

The scattered light signals of particles were then captured by six CMOS cameras (4 Photron SA-4 and 2 Photron SA-1.1) as shown in Figure 2-1. All cameras were aligned in the *x*-*y* plane so that their orientations were specified by θ, defined as the angle formed by the optical axis of a camera relative to the positive *x* direction as shown in Figure 2-1. The focal length and *f*-number of the lenses used on all cameras were 105 mm and 2.8, respectively. The operation of the laser and cameras was synchronized using control electronics, and the camera control and projections acquisition were centralized on a computer. All six cameras were operated at a repetition rate of 1 kHz and an exposure time of 1 ms. Prior to any measurement, a view registration (VR) process was performed to determine the orientations and locations of the cameras relative to the solid sample. The VR process involved a calibration target with known and precise patterns, and a camera calibration program as detailed in [43, 44]. The view angles of camera 1 through 6 were determined to be θ =219.5°, 270.0°, 315.7°, 50.1°, 118.6° and 139.0°, respectively, with an average VR error of ±0.3° [45]. These view angles were selected to 1) maximize the linear independence of the projections following the method outlined in [46], and 2) minimize exposure to reflected light. A VR error of ±0.3° corresponds to an uncertainty of ±0.3 pixel for the setup in this work as to be elaborated later. Here the VR error was defined as the difference between the true view angle versus that determined by the VR process experimentally. The horizontal distance from the lenses to the center point of the breadboard was measured to be 439 mm and the magnification ratio is 0.31.

2.3 Experimental results

Figure 2-2 shows a pair of example projections of the controlled cell measured by camera 1 and 4. Each projection had 900 × 300 pixels (cropped from the original CMOS image with 1024 × 1024 pixels), and each pixel corresponded to a physical dimension of ~0.06 × 0.06 mm^2. As mentioned before, the projections were captured with a frame rate of 1 kHz and an exposure time of 1 ms. These measurements were static (since neither the controlled cell nor the particles were moving during the exposure time), and the primary reason of picking the frame rate and exposure time was to ensure sufficient scattering light signals. Figure 2-2a and Figure 2-2b show the nature of the scattering signal and the particle distribution from two different perspectives. As can be seen, the densities of the particles varied from region to region on the same camera (and also from camera to camera too), primarily due to the line-of-sight-integration effects generic to volumetric measurements, and this will be further elaborated using the results from Figure 2-3 below. Note that Figure 2-2 also shows multiple vertical lines on the raw projections, and these lines corresponded to the edges of glass plates. The method that we found effective in removing the artifacts involved two steps. First, we directly used the raw projections as shown in Figure 2-2 to perform the reconstruction. We did not attempt to remove them via post-processing methods from the raw projections because some of them were embedded in the signal as seen. Second, in the reconstruction, these vertical lines were manifested as planes that were located at the boundaries of the measurement volume. Thus, these planes were then easily identified, separated, and removed from the reconstruction.

Figure 2-3 shows the example particle image density distributions of the projections taken by camera 1 and 4 in terms of particles per pixel (i.e., ppp). The ppp distribution was estimated in three steps using the Analyze Particles function in ImageJ. More specifically, first, for a given pixel on which the ppp is to be estimated, a sliding window with a size of 7×7 pixels was formed centering on the target pixel. Second, this sliding window was binarized using the entropic thresholding method detailed in [47] and the binarized particles in the sliding window were counted. Third, the average ppp within the sliding window was calculated as the ppp of target pixel. The above steps were applied on each pixel individually for a projection captured by a camera to obtain the distribution shown in Figure 2-3. Though note that for tomo-PIV, the concept of ppp is more intricate to interpret than in the case of planar PIV due to the different line-of-sight integration effects from different orientations. Therefore, the ppp distribution varies significantly from region to region and from camera to camera significantly as seen in Figure 2-3, and the 0.08 ppp was an average from all the projections used in this work (compared to the highest particle density of ~0.19 ppp which occurred near the region around pixel (524, 237) on camera 4 as shown in Figure 2-3b). A well-recognized issue in PIV measurements involves resolving overlapping particles [8, 48, 49], and the particle image density shown in Figure 2-3 is an intuitive diagnosis tool for evaluating the severity of overlapping issue. However, our results show the particle image density depends on the orientation for a multi-camera setup as mentioned, and also that the ability to resolve overlapping particles depends on the number of cameras used (more cameras enable enhanced ability to resolve overlapping particles). A systematic examination of such dependences is of great interest and importance, however is beyond the scope of this work and will merit a separate treatment.

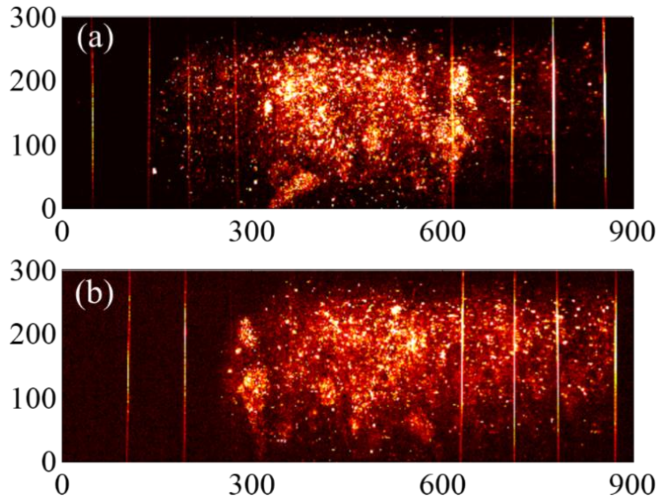

Figure 2-2 A set of scattering signal of particles taken by camera 1 (panel (a)) and 4 (panel (b)), respectively.

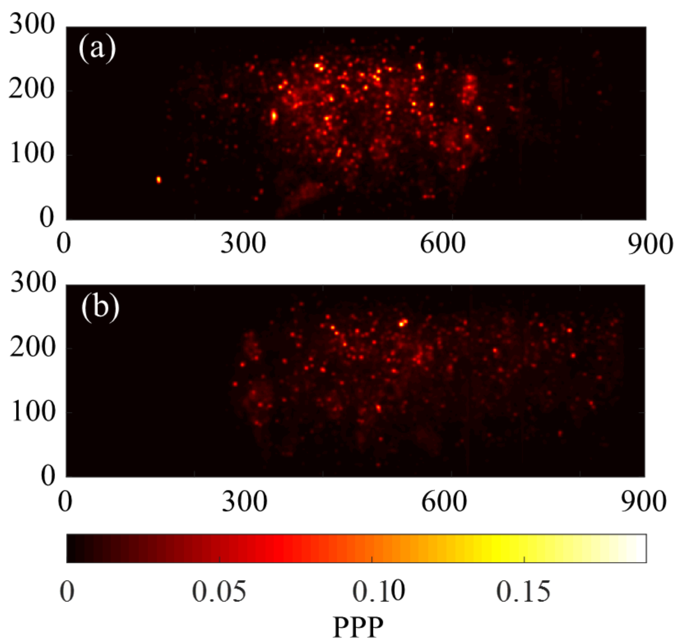

Figure 2-3 A set of PPP distributions of projections taken by camera 1 (panel (a)) and 4 (panel (b)), respectively.

Based on the projections of all cameras, a tomographic reconstruction of 900 × 900 × 300 voxels was performed to obtain the scattering light distribution of the cell using a Multiplicative Algebraic Reconstruction Technique (MART) [50] with 20 iterations and a relaxation factor of 1 [8]. The MART algorithm used here is a variation of the Algebraic Reconstruction Techniques (ARTs) as detailed in [51], and the algorithm performs tomographic reconstruction by adjusting the reconstructed fields to match the measured projection at each camera sequentially and iteratively until converging on a solution. The MART algorithm was executed on a workstation with 16-Core Intel Xeon 2.6GHz and 512 GB memory, and it took a computing time of ~36 hours for each reconstruction to converge with the voxel set in this work.

Equipped with such tomographic algorithm, the 3D distribution of particles can be reconstructed, and then denoted as the particle distribution at initial position. Starting from the initial position, the location of the cell was moved by the stage to create a displacement for the particles. Experimentally, two types of movement were used in this work, the first one by a translation of 0.51 mm towards the positive x direction, and the second one by a clock-wise (viewed from the top) rotation of 2.5° around the cell center. Such translation and rotation were designed based on two considerations. The first consideration was to minimize them to explore the performance limit of tomo-PIV in resolving particle motion. The second consideration was that they need to be large enough to be resolvable by the experimental setup in this work. More specifically, the finest resolvable motion was limited by the camera with the most unfavorable view orientation (which was camera 6, whose optical axis was closest to 90°, among all cameras used, with respect to the sample plane).

For each new position, the projections were recorded again and the corresponding tomographic reconstruction performed. After the position of particle distributions at consecutive locations (equivalent to times) were obtained, a 3D cross correlation algorithm [8] was applied to obtain the displacement field based on the two reconstructed particle distributions. The 3D cross correlation algorithm used here is a straightforward extension of established 2D cross correlation algorithms. More specifically, the 3D algorithm was implemented in two steps. First, the 3D cross correlation of two particle position distributions was calculated within 30×30×30 voxel interrogation volumes at 75% overlap following the suggestion from [2] to obtain a correlation matrix. Second, each displacement vector is determined by subtracting the dimensions of interrogation volume from the voxel location of the maximum element in the resulting correlation matrix. Under this setup, the number of particles was on the order of ~210 per interrogation volume on average, and the effective image density per planar slice in the volume was ~7 on average. This level of effective image density was close to the minimum requirement suggested in [1] for a reliable 3D cross correlation.

With the above description of 3D cross correlation, a measured displacement field containing 117 × 117 × 37 vectors was acquired. Figure 2-4 shows the vector distribution of the displacement field of the translation (Figure 2-4a) and rotation (Figure 2-4b) movement. As shown in Figure 2-4, the overall motion pattern was well captured for both the translation and rotation cases. Figure 2-4a shows that majority of the three components of displacement vectors were equal or close to (8 voxels, 0, 0), corresponding to the physical distance of 0.51 mm along the *x* direction. Figure 2-4b shows that the distribution of vectors followed a rotational pattern around the measurement volume center as expected.

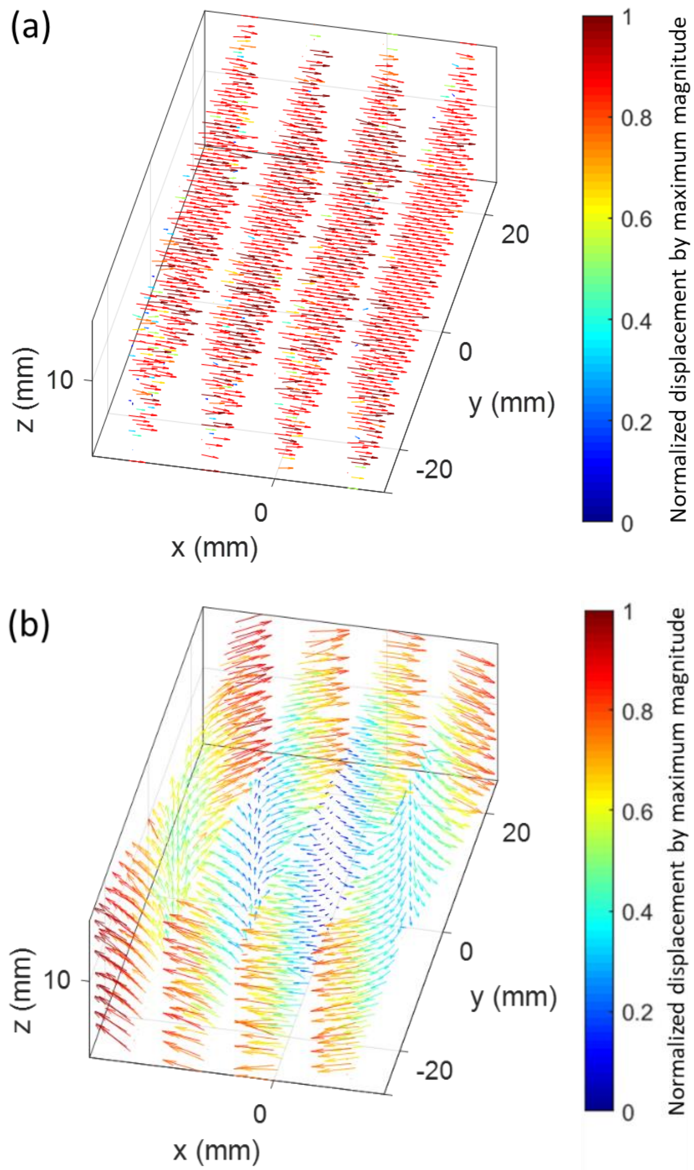

Figure 2-4 The vector distribution of the displacement field of translation (panel (a)) and rotation (panel (b)) measurement.

To provide further insights to the accuracy of the displacement vector distribution shown in Figure 2-4, numerical simulations were performed in parallel with the experiments.

These numerical simulations were performed in the following four steps. First, a phantom was created to simulate the distribution of particles in the controlled cell. For the sake of simplicity, we used the intensity distribution of the reconstruction obtained at the initial position in the experiment as the phantom. Second, the phantom was moved either translationally by 8 voxels towards the *x* direction (to simulate the translation experimental measurement) or rotated clock-wise by 2.5° (to simulate the rotational experimental measurement), creating the corresponding new phantom at the updated position. Third, projections of both phantoms at the initial and the updated positions were calculated at the same orientations as used in the experiments, during which artificial noises were added to simulate possible measurement uncertainty of the experiments. These calculations were performed using a method combining ray-tracing and Monte Carlo simulations as detailed in our earlier work [46, 52]. Two primary sources of noise were considered in this work (which should be representative for tomo-PIV measurements in general): background (BG) noises and noises from the view registration process. The VR uncertainties was considered by the ray-tracing program, and the BG noises were considered by adding white noise to the simulated projections. In the fourth step, the projections calculated during the third step were used as inputs to the MART algorithms to solve for the positions of the particles at the initial and update locations. And in the final fifth step, these positions were correlated to obtain the velocity fields.

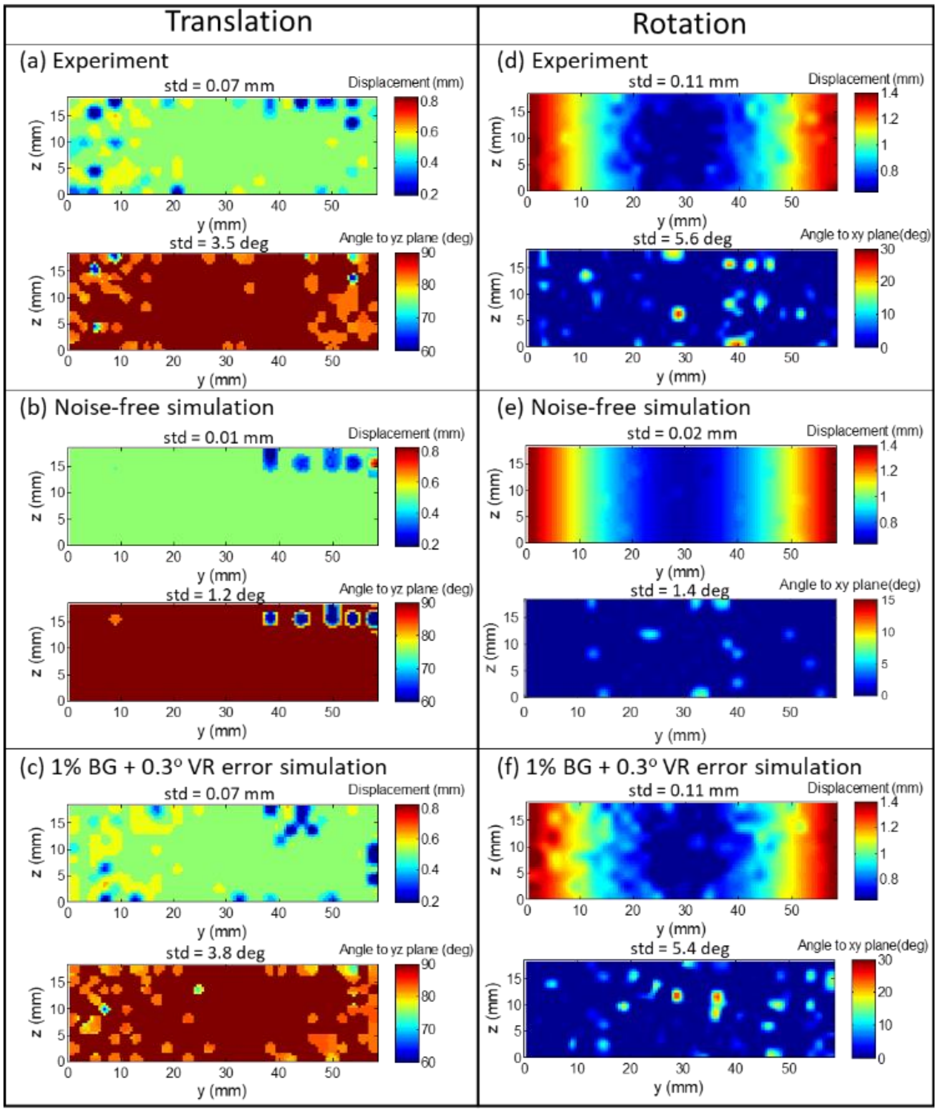

Figure 2-5 Comparison of experiment and simulation results of transition measurements on displacement vector magnitude and angle relative to the yz plane (Panel (a), (b) and (c)), and rotation measurements on displacement vector magnitude and angle relative to xy plane (Panel (d), (e) and (f)).

Figure 2-5 summarizes the results from these simulations to provide a quantitative analysis of the experimental results. Figure 2-5a evaluates the displacement and vector fields of translation and rotation measurements in a 2D plane. Such 2D plane corresponds to the glass piece located at x = -33.50 mm, the leftmost piece as shown in Figure 2-1. Figure 2-5a shows the distribution of the displacement magnitude (i.e. vector norm) and angle of vectors relative to the *yz* plane calculated from the 3D3C measurements. The true value of the displacement magnitude and angle were 0.51 mm and 90º, respectively. As shown in Figure 2-5a, the majority of magnitudes were measured experimentally precisely, and the errors appeared primarily around the boundary of the measurement plane. The averaged errors of magnitude and angle to the *yz* plane for the translation experiment as shown in Figure 2-5a were calculated to be 0.8 voxel and 1.7°, suggesting an overall good measurement accuracy. To obtain further insights into the experimental, Figure 2-5b shows a numerical simulation with conditions replicating the experimental conditions less any noise (i.e., noise-free ideal experiments). As expected, Figure 2-5b shows a more uniform distribution of displacement magnitude and angle with only a few larger errors, also located around the boundary of measurement plate. The errors seen in Figure 2-5b were caused purely by the MART algorithm, and the differences between Figure 2-5a and 2-5b were due to experimental uncertainties. To further quantify the experimental uncertainties, numerical simulations were performed with various levels of measurement uncertainties artificially added to the projections. Two categories of uncertainties were considered here: background (BG) noises and view registration (VR) uncertainties. Based on such contaminated projections, reconstructions were obtained and error distributions calculated. The goal was to search for the level of BG and VR errors that could best reproduce (i.e., fit) the experimental results observed. Figure 2-5c shows the simulation results obtained with 1% BG and 0.3° VR uncertainty added into the simulation. A comparison between

Figure 2-5a against 2-5c (and also between Figure 2-5d and 2-5f too for the rotational case) shows that the error distributions from the experimental results were statistically the same as those from the simulation results with 1% BG and 0.3° VR error. Such comparison suggested that 1% BG noise and 0.30 VR uncertainty could be a reasonable estimate of the error sources in the measurements, which were in reasonable agreement with our experiences. In addition, Figure 2-5 also provides the standard deviations of the magnitude and orientation of the displacement for both the experiments and simulations results. These statistics are shown right above each plot. For example, for the translation cases as shown in Figure 2-5a and 2-5c, Figure 2-5a shows the standard deviations of the magnitude and the angle to the *yz* plane were 0.07 mm and 3.5^0 for the experimental results, in close agreement with 0.07 mm and 3.8^0 obtained for the simulation results with 1% BG and 0.3^0 VR uncertainty as shown in Figure 2-5c.

Parallel to the results shown for the translational cases above, Figure 2-5d ~ 2-5f show the experimental results and their analysis for the rotational cases. As shown in Figure 2-5d ~ 2-5f, the magnitude distribution was measured on another piece of glass located at x = 18.50 mm, corresponding to the rightmost piece as shown in Figure 2-1. For Figure 2-5d ~ 2-5f, the distribution of displacement magnitude and angle of vectors relative to the *xy* plane were calculated. As aforementioned, the measurement domain was rotated in the *xy* plane around the center at the origin. Therefore, the true displacement magnitude was perfectly symmetrical about y = 0 mm and constant along the z direction, and the true value of the angle of the velocity vector relative to the *xy* plane should be 0°. Several observations can be made from these results. First, the average errors of magnitude and angle to the *xy* plane for the rotation experiment as shown in Figure 2-5d were determined to be 1.4 voxels and 1.9°. Second, as shown in Figure 2-5e, the noise-free simulation presents nearly ideal distribution of displacement magnitude and angle, while Figure 2-5d and 2-5f both show notable non-uniformity in the displacement and angle distribution, especially near the center of the measurement plane. One possible reason is that the displacement vectors near the plane center have smaller magnitude, thus are more sensitive to the measurement error. Similar to the above analysis of the error and the related standard deviation made for the translational cases, the simulation with 1% BG and 0.3° VR error for the rotational case reproduced the experimental results the best, supporting that these BG and VR uncertainties to be a reasonable estimate of the experimental uncertainty.

To further examine the above analysis of the experimental uncertainties, Figure 2-6 show a more detailed comparison between the experimental and the simulation results with 1% BG and 0.3^{o} VR uncertainty by plotting the percentage distribution of the errors. Figure 2-62-6a and 2-6b show the percentage distribution of the displacement magnitude error for the translation and rotation measurements, respectively. The displacement magnitude error here was calculated by firstly subtracting the measured displacement vector from its ideal vector, and then calculating the norm of the subtracted vector. Figure 2-6c shows the percentage distribution of angle of vectors to *yz* plane for translation measurement. Figure 2-6d shows the percentage distribution of angle of vectors to the *xy* plane for rotation measurement. As can be seen from Figure 2-6, for the results under all panels, the detail percentage distribution of the simulated error match the experimental results with reasonable agreement. Again, this comparison supports that 1% BG and 0.3° VR error were reasonable estimates of the experimental uncertainty. It is typically difficult, if possible at all, to isolate and quantify various sources of experimental uncertainties. The simulation results and method discussed here served as an effective approach, and we expected them to provide insights to aid the interpretation of tomo-PIV experiments.

As a next step, numerical simulations were performed to further explore the effects of VR uncertainties, and the results are shown in Figure 2-7. These simulations were performed with the BG noise fixed at 1% while the VR noise was varied from 0.1° to 0.6°. These simulation studies were motivated by the practical consideration that BG noise is difficulty, if possible at all, to be controlled or reduced, while there are possible approaches to improve the VR process and reduce the VR noise[45, 53-55]. Figure 2-7a and 2-7b show the displacement magnitude error distribution of the simulated translation and rotation measurements, respectively. Figure 2-7c and 2-7d show the error distribution of the vector angle of the simulated translation and rotation measurements, respectively. Several observations can be made based on these results. First, for the noise-free simulation shown in Figure 2-7a and 2-7b, more than 95% of the velocity vectors were reconstructed with no displacement error in the translational case, and the more than 87% reconstructed with no displacement error in rotational case. Such results obtained from noise free simulation were consistent with the experimental results discussed earlier, showing that it was more difficult to reconstruct the magnitude of the velocity vectors accurate for rotational velocity fields than for translational fields. Such noise-free results shown in Figure 2-7a and 2-7b also illustrate the level of reconstruction error brought about by the MART algorithm itself, suggesting the potential for algorithm improvement. Second, for error in the vector, Figure

2-7c and 2-7d show that, under the noise-free case, more than 96% of the vectors were reconstructed with no error for both the translational and rotational fields. Such results were again consistent with the experimental results discussed earlier, suggesting that it is equally difficult (or easy) to obtain the correct velocity vector orientation in both translational and rotation velocity fields. Third, it can be seen that more vectors were reconstructed with increasing errors as the noise level increased. As one example, Figure 2-7a and 2-7b show that less than 1% of the velocity vectors were reconstructed with a magnitude error at 0.38 mm with 0.3^0 VR error, compare to almost 10%, a more than 10x increase, when the VR error increased to 0.6^0. As another example, for the noise-free cases, Figure 2-7c and 2-7d show that no vector was reconstructed with an angle error more than 10°, and less than 5% of vectors were reconstructed with an error larger than 5°. However, with 1% BG and 0.3° VR noise, angle error up to 30° began to occur (also consistent with the experimental results discussed earlier).

These results suggested that the VR error impacts the reconstruction accuracy significantly, motivating future research to develop improved VR processes to reduce the VR error. The results in Figure 2−7 shows that if the VR error can be reduced to the level of 0.1^0, the overall reconstruction error will be significantly reduced, and also the larger errors will be removed. Specifically, for the cases studied here, as the VR error was decreased from 0.6° to 0.1°, the tomo-PIV accuracy was improved by at least 2.5× in terms of both displacement vector magnitude and orientation. The magnitude error was reduced from 1.5~2.1 voxels to 0.5~0.8 voxels, and angle error reduced from 4.5°~3.8° to 0.6°~1.3° for the translational and rotational velocity fields, respectively.

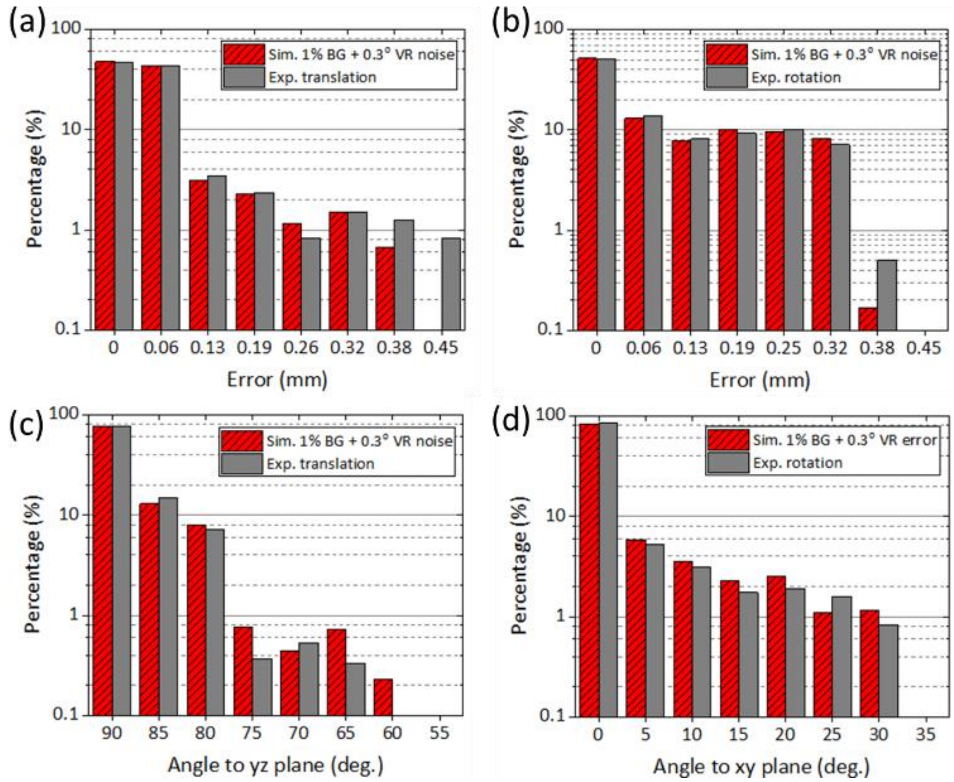

Figure 2-6 Percentage distributions of experiment and simulation results with 1% BG and 0.3° VR noise. Panel (a) and (b): displacement error for translational and rotational velocity fields, respectively. Panel (c): angle of vectors relative to the yz plane for translational velocity fields. Panel (d): angle of vectors relative to the xy plane for translational fields.

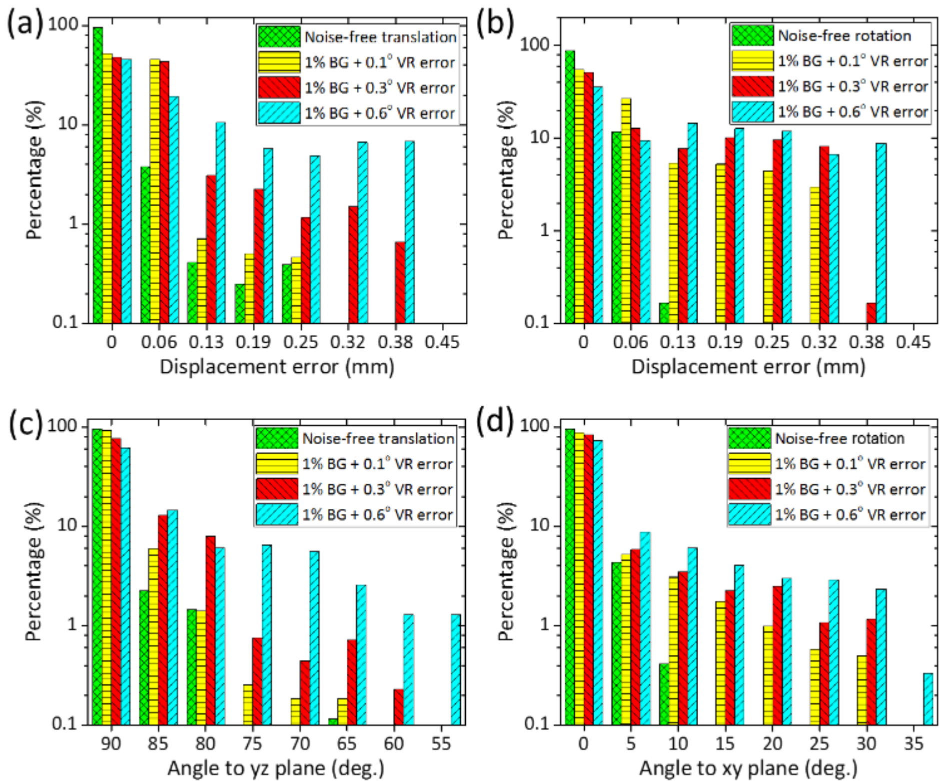

Figure 2-7 Percentage distributions of simulation results with different compositions of noise. Panel (a) and (b): displacement error for transitional and rotational fields, respectively. Panel (c): angle of vectors relative to yz plane for translation. Panel (d): angle of vectors relative to xy plane for rotation.

2.4 Summary

In summary, this work reports the experimental validation of tomographic particle image velocimetry (tomo-PIV) for measuring 3D3C velocity fields using controlled tests. This work designed a method involving solid samples to create precisely controllable particle displacement fields to simulate flow fields. The displacement fields were experimentally measured by a six-camera tomo-PIV system, and the experimental results then analyzed to quantify the accuracy of 3D3C velocity fields obtained from the tomo-

PIV technique. The results obtained in this work quantified the capabilities and uncertainties of tomo-PIV for resolving the magnitudes and orientation of 3D3C velocity fields. More specifically, the major observations can be summarized into the follow three aspects. First, the results showed that tomo-PIV technique was able to reconstruct the 3D3C velocity with an averaged error of 0.8 to 1.4 voxels in terms of magnitude and 1.7° to 1.9° in terms of orientation for the velocity fields tested. Second, these results illustrated that the view registration (VR) process plays a significant role in tomo-PIV. By reducing VR error from 0.6° to 0.1°, the overall 3D3C measurement accuracy can be improved by at least 2.5× in terms of both magnitude and orientation, and also the larger outliers of reconstruction errors can be removed. Since there are possible methods to improve the VR process, these results provide motivation for further investigation of these possibilities. Third, the use of additional cameras in tomo-PIV can extend the 3D3C velocity measurement to a larger volume while maintaining acceptable accuracy (that is, at the cost of increasing equipment cost). With the six cameras used in this work, 3D3C measurements were obtained in a volume with a thickness of 57 mm in the direction of the field-of-view of the cameras. In comparison, the thickness of the measurement volume was typically on the order of ~25 mm with a four-camera setup predominately applied in the past. We expect these results and observations to aid the error analysis and the design of tomo-PIV measurements.

Chapter 3 Regularized tomo-PIV based on conservation of mass

Abstract

3D3C (three-dimensional and three-component) velocity measurements have long been desired to resolve the 3D spatial structures of turbulent flows. Recent advancements have demonstrated tomographic particle image velocimetry (tomo-PIV) as a powerful technique to enable such measurements. The existing tomo-PIV technique obtains 3D3C velocity field by cross-correlating two frames of 3D tomographic reconstructions of the seeding particles. A most important issue in 3D3C velocity measurement involves uncertainty, as the derivatives of the measurements are usually of ultimate interests and uncertainties are amplified when calculating derivatives. To reduce the uncertainties of 3D3C velocity measurements, this work developed a regularized tomo-PIV method. The new method was demonstrated to enhance accuracy significantly by incorporating the conservation of mass into the tomo-PIV process. The new method was demonstrated and validated both experimentally and numerically. The results illustrated that the new method was able to enhance the accuracy of 3D3C velocity measurements by 40~50% in terms of velocity magnitude and by 0.6~1.1° in terms of velocity orientation, compared to the existing tomo-PIV technique. These improvements brought about by the new method are expected to expand the application of tomo-PIV techniques when accuracy and quantitative 3D flow properties are required.

3.1 Introduction

Instantaneous 3D3C (three-dimensional and three-component) velocity measurements represent an ultimate goal of velocimetry, which is to fully resolve unsteady flow structures. However, it was only recently that substantial progress in instantaneous 3D3C velocimetry has been made owing to the advancements in lasers, digital imaging, and computational technology [17, 22, 56]. In the recent past, several approaches have been demonstrated to enable 3D3C velocity measurements, including scanning particle image velocimetry (PIV) [3, 5, 57, 58], holographic PIV [6, 7, 59], and tomographic PIV (tomo-PIV) [8, 22, 26, 60, 61]. A comprehensive comparison of these approaches is beyond the scope of this paper, and interested readers are referred to [17, 22, 56] and the references therein.

This current work focuses on the tomo-PIV technique. Tomo-PIV obtains 3D3C velocity measurements by combining PIV measurements with 3D tomographic reconstruction. Conceptually, this technique involves two steps. In the first step, the distributions of seeded particles in 3D are obtained at two consecutive times using 3D tomographic reconstructions. At each time, a thick laser slab is used to illuminate the seeded particles volumetrically, and multiple cameras are used to capture the scattered signal from different orientations, providing the inputs for a tomography algorithm to obtain the 3D distribution of the seeded particles. In the second step, a 3D3C velocity field is calculated by performing a cross-correlation of the two frames of 3D particle distributions obtained in the first step. Such tomo-PIV technique has been demonstrated [8, 61, 62], validated [19, 60, 63], and applied to investigate a variety of flows [24, 25].

The second step is a relatively straightforward extension of established 2D PIV correlation. However, the first step presents significant additional complexity and uncertainty to the measurements compared to 2D PIV measurements. For instance, due to the nature of the volumetric illumination and the use of multiple cameras, it becomes important to calibrate these cameras both in terms of their noise level and their relative orientation. Such calibration inevitably involves uncertainties, including camera noise and also orientation error [19], and these uncertainties propagate through the rest of the data processing. Also, the subsequent tomography algorithm can only reconstruct with a finite accuracy even if the measurements captured by the cameras are error free. In practice, these measurements are contaminated by noises (e.g., due to the calibrations just mentioned), and such noises will propagate (or even become amplified) during the tomographic reconstruction process. As a result, accuracy of tomo-PIV can be much worse than that of 2D PIV, while accuracy is of paramount importance in many velocity measurements as their derivatives are of ultimate interest to determine quantities such as vortex, force, energy, etc. Currently, the measurement accuracy of 3D3C velocity enabled by tomo-PIV was reported to be on the order of ~1 voxel and ~2° in terms of velocity magnitude and direction [19], respectively; in contrast, the 2D PIV technique can yield a measurement accuracy of ~0.5 pixel and ~1° [20, 21].

Recognizing the additional complexity brought about by tomo-PIV and the critical need for accuracy, considerable efforts have been made to enhance the measurement accuracy of tomo-PIV from tomography reconstruction (step 1) and cross-correlation (step 2). The investigation of tomography reconstruction included a range of experimental and computational efforts to improve the reconstruction accuracy. Experimental effects included the optimization of key imaging parameters [22, 23, 64], tomography imaging configuration (cross-like configuration [24, 25] and linear configuration [26, 27]), view registration [28-30], seeding density [31, 32], etc. In parallel, computational efforts included optimization of existing reconstruction algorithms such as ART (algebraic reconstruction technique) and MART (multiplicative algebraic reconstruction technique) [8, 33], the use of spatial filter in the reconstruction [33], the integration of sparsity maximization into reconstruction [34, 35], and the development of new reconstruction methods and algorithms [29, 36, 37], etc. In addition to the investigation in tomography reconstruction, significant efforts have also been invested in the improvement of the second step, the cross-correlation step. Examples include the development of high-accuracy cross-correlation algorithms such as the 3D window deformation algorithm [38], methods for sub-voxel estimation [5], and the use of low-pass filters in 3D image pre-processing [39].

The focus of this work involves the second step. Based on the above understanding of past efforts, this work describes a new approach to improve the cross-correlation by incorporating flow physics. It is intuitive to recognize that if some fundamental flow physics can be integrated into the cross-correlation process (e.g., as a regularization), it has the potential to improve the accuracy and can lead to more accurate velocity vectors. Based on such recognition, this work investigated a regularized tomo-PIV method (code-named RTPIV) using the conversation of mass as a regularization for incompressible flows. The rest of this chapter describes the development of the RTPIV method in detail (Chapter 3.2), and also presents the confirmation and demonstration results obtained both by controlled experiments and by numerical simulations (Chapter 3.3). Finally, Chapter 3.4 will conclude the work with a summary of the major observations, a discussion of the limitations of the current work, and possible directions for further study.

3.2 Problem formulation and algorithm description

This section describes the mathematical formulation of the proposed RTPIV method. As described in Section 1, the first step in tomo-PIV involves obtaining the 3D distribution of the seeded particles (denoted as F) using tomographic reconstructions. The 3D tomographic reconstruction to obtain F has been previously detailed elsewhere [10], and only a brief summary is provided here to facilitate the discussion of the regularized cross-correlation process. After discretization of the measurement domain into voxels, the relationship between the projections measured by the cameras and the sought F is related by the following equation:

$$\boldsymbol{P} = \boldsymbol{PSF} \cdot \boldsymbol{F} \tag{3-1}$$

where $\boldsymbol{P}$ represents all the measured projections organized into a vector format pixel by pixel, $\boldsymbol{F}$ the discretized particle distributions also in vector format by organizing its values voxel by voxel, and $\boldsymbol{PSF}$ the point spread function matrix that only depends on the geometry parameters of the imaging system used (i.e., no dependence on $\boldsymbol{F}$) [65, 66]. The algorithm used to solve Equation 3-1 in this work was the Multiplicative Algebraic Reconstruction Technique (MART) as detailed in [19, 51].

In practice, Equation 3-1 was solved twice with two sets of projections captured by cameras at two consecutive times to provide the corresponding particle distributions (denoted $\boldsymbol{F}_1$ and $\boldsymbol{F}_2$). The resultant $\boldsymbol{F}_1$ and $\boldsymbol{F}_2$ are then cross-correlated to provide the final 3D3C velocity.

To reduce the uncertainties of 3D3C velocity measurements induced both by the reconstruction step and the cross-correlation step, this work describes a new method, code-named RTPIV, to incorporate the conservation of mass (COM) equation as *a priori* information into the cross-correlation. For divergence-free flows (i.e., incompressible flows), the COM equation is simplified to $\nabla\cdot\boldsymbol{V}=0$. Therefore, for such flows, instead of simply correlating $\boldsymbol{F}_1$ and $\boldsymbol{F}_2$ to solve for velocity ($\boldsymbol{V}$) as practiced in past work, this work solves for velocity through the following minimization problem:

$$\min\ E = \alpha\bullet\sum\left|\nabla\bullet\boldsymbol{V}\right| + \sum(-\mathrm{CC}(\boldsymbol{V})) \tag{3-2}$$

where E is the master function to be minimized, $|\nabla\cdot\boldsymbol{V}|$ is the regularization term, i.e., the modulus of the velocity divergence, $\mathrm{CC}(\boldsymbol{V})$ is the value of cross-correlation under a given velocity vector, and α is the regularization parameter used to adjust the weights of these two terms. The summation in Equation 3-2 runs over all the velocity vectors obtained in the discretized domain. Since $\boldsymbol{V}$ is obtained based on the reconstructed $\boldsymbol{F}_1$ and $\boldsymbol{F}_2$, the minimization of Equation 3-2 ultimately relies on both the COM regularization and the tomographic measurements. Note that the negative sign in front of the cross-correlation term in Equation 3-2 is needed so that minimizing Equation 3-2 is equivalent to maximizing the cross-correlation. Also, the modulus of the divergence in Equation 3-2 is used to ensure a positive regularization term to be minimized.

The formulation in Equation 3-2 enables the simultaneous consideration of *a priori* information (i.e. the COM equation) and *a posteriori* information (i.e., the measurements). Conceptually, the ideal solution from solving Equation 3-2 is the one that makes the first term zero (such that the COM equation is perfectly satisfied), and at the same time maximizes the second term (such that optimal correlation is achieved with the measured data). In practice, due to the presence of noises, both experimental and numerical, the solution from Equation 3-2 will not perfectly satisfy the COM equation or maximize the cross-correlation of the measurements. Instead, the solution will be a balanced consideration of both. The regularization parameter, α, controls the relative weight of them and therefore is a key parameter – not only for this particular RTPIV problem, but for regularized schemes in general [67, 68]. This work employed the so-called L-curve method to determine the optimal α [69], which is to be elaborated in detail in the next section.

Before describing the specific methods for solving Equation 3-2, note that the particular formulation shown in Equation 3-2 only applies to incompressible flows. For other types of flows (e.g., compressible flows, multiphase flows and most reacting flows), the COM equation can involve other properties beyond velocity. There are possible approaches that the COM equations can be incorporated into the reconstruction process for these flows, but modifications and extensions of Equation 3-2 will be needed. In this work, we limit our focus to incompressible flows, and want to emphasize that incompressible flows already represent a wide range of applications of contemporary interests (such as the study of many bio-induced flows and the operation of many unmanned aerial vehicles where small-scale vortices and erratic velocity components exist). Furthermore, the current RTPIV method could be applied to certain reacting flows when the density variation is negligible.

The problem formulated in Equation 3-2 represents a global minimization problem that is not always easy to solve numerically, due to the complexity of velocity fields that can create interfering local minima. This work adopts the Simulated Annealing (SA) algorithm due to its robustness. SA is a probabilistic algorithm [70] that has been demonstrated to solve a range of difficult minimization problems with numerous interfering local minima [53, 71].

With these above understandings, this work has developed the following four steps to solve Equation 3-2 to obtain 3D3C velocity, as summarized by the flow chart in Figure 3-1. In the first step, tomo-PIV reconstruction was performed in a traditional way following [8, 24], and the solution was used to initialize the 3D3C velocity field and the master function *E*. More specifically, the reconstructions of particle distributions across two consecutive frames were used to compute the correlation on each integration volume (IV) and then the summation $\Sigma(-CC(\boldsymbol{V}))$ over all IVs. The velocity vectors were used to calculate $|\nabla\cdot\boldsymbol{V}|$ on each IVs using the central difference scheme (with a second-order accuracy of the discretization), and then $\Sigma|\nabla\cdot\boldsymbol{V}|$ over all IVs. Once the correlation term and divergence were both obtained, they were added to initialize the master function *E*. In the second step, the velocity field initialized in the first step was adjusted. The adjustment was performed by applying a random amount of perturbation to the three components of the initial velocity vectors, and the perturbed 3D3C velocity field was denoted by $\boldsymbol{V'}$. The resultant $\boldsymbol{V'}$ was then used to update the master function *E*, and the updated value of *E* was denoted as *E'*.

In the third step, *E'* was compared to *E* by the Metropolis criterion [70] to decide whether the adjusted velocity field (i.e., ***V'***) should be rejected or accepted. If the decision was to reject, then the initial velocity field was adjusted again to form another perturbed velocity field. If the decision was to accept, then ***V'*** was regarded as a more accurate velocity field and was used as the starting point for the next round of perturbation. In this step, the use of the Metropolis criterion is the key to the SA algorithm, which allows the RTPIV method to evolve the solution in the most promising direction after exploring possible velocity perturbations from all directions. In the fourth and last step, step 2 and 3 were iterated until *E* converged to a preset criterion. In this work, the criterion was set so that when the relative change of *E* between two consecutive iterations was below 0.1% following the suggestion in [72]. Also, our results showed that the accuracy of RTPIV was insensitive to this preset level. The accuracy of RTPIV changed within 0.5% when the preset level varied between a range of 0.001% to 0.1%.

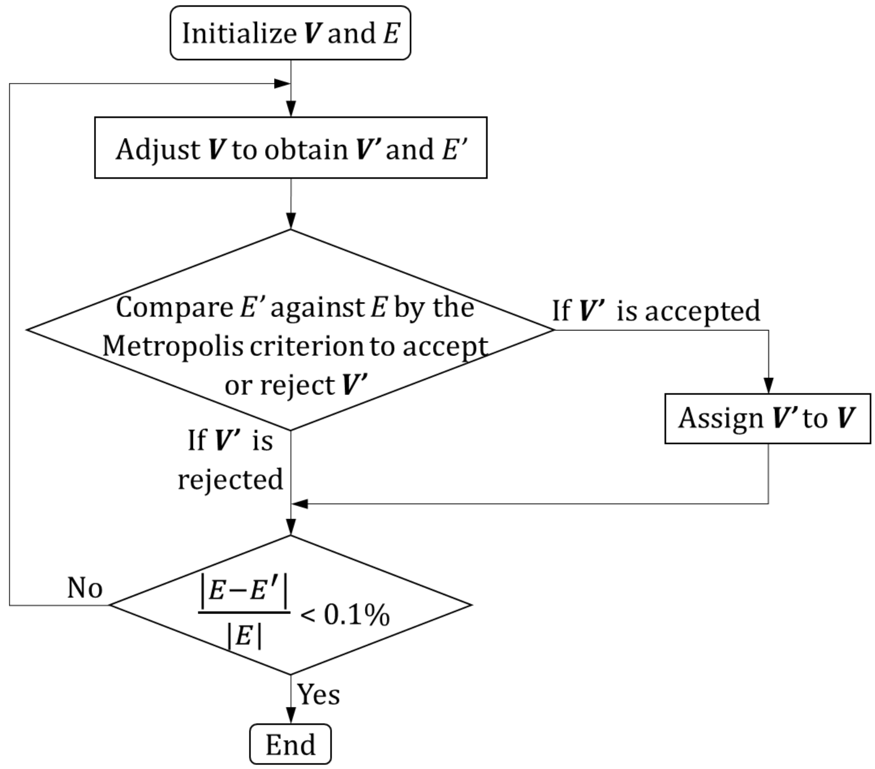

Figure 3-1 Flow chart summarizing the RTPIV method.

3.3 Validation via controlled experiments and numerical simulations

This section describes and demonstrates the validation of the RTPIV method via controlled experiments. The setup for the controlled experiments is illustrated in Figure 3-2. This setup was similar to that described in [19]. The central concept of the experiment involved using a solid sample to create precisely controlled velocity field for validation purposes. More specifically, the experimental setup consisted of three major components as shown in Figure 3-2: a solid sample assembled from thin glass slides, an illumination laser, and a total of 6 CMOS cameras.

As shown in Figure 3-2, the solid sample assembled from thin glasses was placed in the center of the setup. Four pieces of thin glass were coated with polystyrene particles with a nominal diameter of 4.05 μm. These particles were coated on one side of each thin glass with an average spacing of ~0.5 mm. Each glass slide had a thickness of 0.5 mm and a height × width of 65 × 60 mm^2. These four slides of thin glass were then clamped together and assembled to form the solid sample. The glasses were adjusted parallel to each other with a spacing of 5 mm between each other. Such 5 mm spacing was chosen to imitate commonly used measurement dimension (along the normal direction of the glasses) in typical tomo-PIV experiments [22]. The solid sample therefore was essentially a transparent cuboid with particles sandwiched in between. The solid sample was then mounted on a rotation stage (Thorlabs PR01), which was in turn mounted in on a translation stage (OptoSigma TSD-602C). The translation stage can linearly translate along one direction with a resolution of 10 μm, and the rotation stage can rotate continuously within 360^o with a resolution of 5 arcmin. As a result, the solid sample can be moved either translationally or rotationally with precision up to the accuracy of the stages. The corresponding movement of the embedded particles were then used to generate the target velocity fields, with well controlled accuracy, for validation and demonstration purposes.

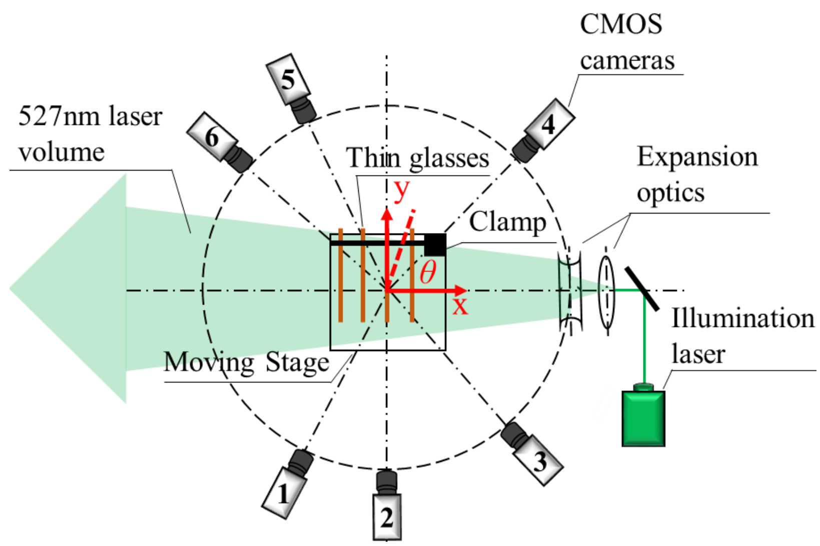

Figure 3-2 Experimental setup.

The second major component was a laser used to illuminate the particles embedded in the solid sample. The laser was a pulsed Nd: YLF laser (Photonics Industries DM30 – 527, labeled as the Illumination laser in Figure 3-2) at a wavelength of 527 nm. The laser pulses were shaped by a series of optics into a thick laser slab to illuminate a measurement volume of 26.4 (*x* direction) × 26.4 (*y* direction) × 12 (*z* direction) mm^3, so that the entire solid sample can be illuminated volumetrically. Based on the controlled cell and laser configuration, a Cartesian coordinate system was defined as shown in Figure 3-2: the center of the translational base was defined as the origin, the plane of the movement of the translational base was defined as the *x*-*y* plane, the direction of the translational movement (also the opposite direction of the laser propagation) was defined as the *x* axis. Essentially, the *x*, *y* and *z* axes were defined along the thickness, width and height direction of the solid sample, respectively.

The third major components involved a total of six cameras to capture the signal from the particles. When illuminated by the laser volumetrically, the embedded particles scattered the incident photons and the scattered photons were then captured by six CMOS cameras (4 Photron SA-4 and 2 Photron SA-1.1) as shown in Figure 3-2. All six cameras were operated with an exposure time of 1 ms, and they were synchronized with the laser using control electronics. All cameras were aligned in the x-y plane within experimental accuracy so that their orientations can be specified by θ (defined as the angle formed by the optical axis of a camera relative to the positive x direction as shown in Figure 3-2). Prior to any measurement, a view registration (VR) process was performed to determine θ as detailed in [73, 74]. The view angles θ of camera 1 through 6 were determined to be 219.5°, 270.0°, 315.7°, 50.1°, 118.6° and 139.0°, respectively, with an average VR error of ±0.3° [75].

With the above setup, two representative controlled experiments were performed to validate the proposed RTPIV method. These two representative experiments involved a translational movement and a rotational movement of the solid sample. For the translational movement, the solid sample was moved 0.51 mm along the positive x axis; and for the rotational movement, the solid sample was rotated clock-wise (viewed from the top) of 2.5° around the cell center. For each experiment, volumetric scattering signals were captured on the cameras before and after the movement, the measured signals were used to reconstruct the 3D distributions of the particles before and after the movement, and velocity field were finally obtained by correlating the 3D particle distributions before and after the movement.

Figure 3-3a shows the 3D3C velocity field reconstructed by the RTPIV method for the translational movements. The reconstruction was obtained with the measurement domain discretized into a total of 440 × 440 × 200 voxels. Under this discretization, two tomography reconstructions at consecutive times were performed using the six projections obtained by the six cameras, each with a pixel resolution of 440 × 200. The tomography reconstructions resulted in two distributions of particle intensities in 3D at two consecutive times. These two distributions were then interrogated using the COM-regularized cross-correlation method as described in Equation 3-2 to generate the ultimate 3D3C velocity field. The COM-regularized cross-correlation was conducted with an interrogation volume of 30 × 30 × 30 voxels at 50% overlap, such that the 3D3C velocity field contained 28 × 28 × 12 velocity vectors as shown in Figure 3-3a. As seen, the obtained velocity vector field captured the uniform nature of the translation movement as expected.

To quantitatively assess the measurement accuracy, the following e_V metric was defined,

$$e_V = \frac{\sum \left| \boldsymbol{V}^{mea} - \boldsymbol{V}^{true} \right|}{\sum \left| \boldsymbol{V}^{true} \right|} \tag{3-3}$$

where V^{mea} and V^{true} represented the measured and true velocity vector, respectively, the $|\cdot|$ sign the modulus of a vector, and the summation operated on a vector-by-vector basis. Conceptually, the e_V defined in Equation 3-3 quantifies the average error of the velocity measured relative to the ground truth. Since the modulus of the velocity vectors was used in the definition, e_V represents the combined effects of measurement error in both the velocity magnitude and also the velocity direction [76]. To decouple such combined effects and explicitly quantify the measurement error in velocity direction, an error of the velocity direction (denoted as e_D) was also defined in this work: e_D was defined as the absolute difference of the velocity direction between the measured velocity vectors relative to the ground truth, averaged across the entire measurement domain. Under these definitions, the e_V and e_D for the measurement obtained by the RTPIV method over the entire domain shown in Figure 3-3a was calculated to be 5.1% and 0.9°, respectively.

To illustrate the advantage of the RTPIV method, the velocity reconstruction was also performed using the traditional TPIV (tomo-PIV) method using the same projection data. The computational settings in the TPIV method remained the same as those used in RTPIV, and the only difference was that it performed the cross-correlation without the COM regularization used in the RTPIV. The e_V and e_D obtained by the traditional TPIV method over the entire domain shown in Figure 3-3a was calculated to be 10% and 1.7°, respectively. Therefore, the new RTPIV method was able to enhance the accuracy significantly both in terms of e_V and e_D (i.e., to 5.1% and 0.9°, respectively). Along with the overall error comparison, the probability density functions (PDFs) of e_V and e_D were also generated by the RTPIV and TPIV methods to provide a more detailed error comparison and further illustrate the superiority of the RTPIV method. Note that a similar level of accuracy enhancements was observed in other cases with different spatial resolutions by varying the interrogation volume (from 16×16×16 voxels to 64×64×64 voxels), too. Then, we examine the results with the current translational velocity field more closely. Figure 3-3b and 3-3c show the velocity vector plots at the central z plane (i.e., z =

6 mm) obtained by RTPIV and TPIV, respectively. Figure 3-3d shows the corresponding ground truth velocity field to be compared to Figure 3-3b and 3-3c directly. The velocity unit as labelled in Figure 3-3b ~ 3-3d was voxel/frame, which was defined as how many voxels the solid sample has been moved between two consecutive frames of tomographic measurements, i.e., before and after the manual movement in this work. As can be seen visually, the enhancement brought about by the RTPIV method resulted in better agreement with the ground truth, and also the significant reduction of vectors with large errors both in terms of magnitude and direction.

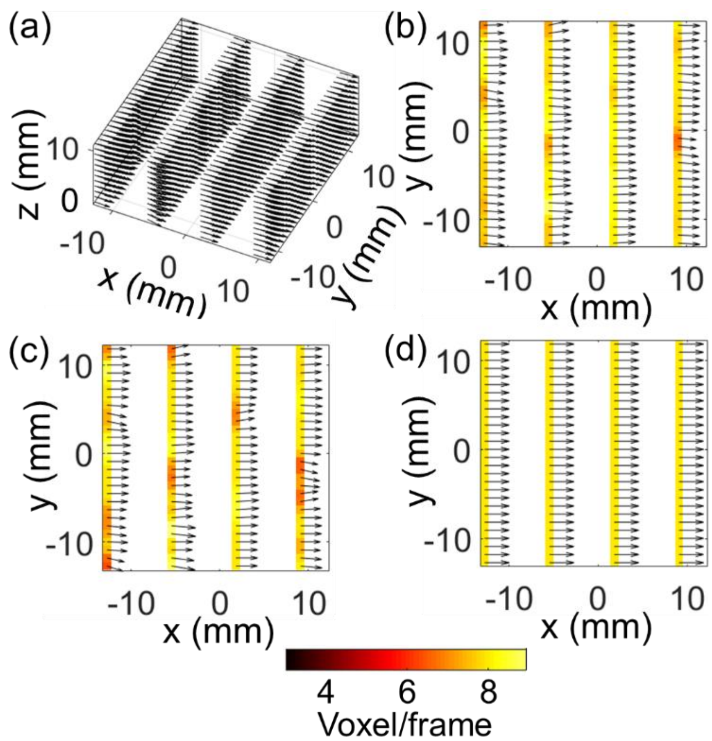

Figure 3-3 Comparison of the RTPIV and TPIV methods using the controlled translation experiment. (a) Velocity vector distribution reconstructed by RTPIV. (b) Reconstructed field by RTPIV at the central *z* plane (*z* = 6 mm). (c) Reconstructed field by TPIV at the same central *z* plane. (d) Ground truth at the same central *z* plane.

Figure 3-4 shows more intermediate steps with the intention of providing more insights to the results in Figure 3-3. Figure 3-4 shows the performance of the RTPIV method when Equation 3-2 was solved with varying α, the regularization parameter. Figure 3-4a shows the value of $\Sigma(-CC(V))$, i.e. the second term in Equation 3-2, versus $\Sigma|\nabla\cdot V|$ when Equation 3-2 was solved at different values of α ranging from 0 to $+\infty$. Here $\Sigma(-CC(V))$ was scaled into a range of [0, 1]. As seen in Figure 3-4a, the curve resulted from such analysis featured an overall approximate L shape, a feature common to regularized techniques in general [69, 71]. The reason for the general L-shape can be intuitively understood by examining its trend at extreme values of α. At one extreme when α =0 (or close to zero), $\Sigma(-CC(V))$ reaches its minima and $\Sigma|\nabla\cdot V|$ is large because Equation 3-2 ignores $\Sigma|\nabla\cdot V|$ and only attempts to minimize $\Sigma(-CC(V))$, as displayed by the nearly horizontal portion of the curve on the lower right corner of Figure 3-4a. At the other extreme when $\alpha = +\infty$ (or very large), the opposite happens: $\Sigma(-CC(V))$ is large and $\Sigma|\nabla\cdot V|$ reaches its minima, as displayed by the nearly vertical portion of the curve on the upper left corner of Figure 3-4a. As α varies in between, the curve traces an overall L shape. Hence, the L curve shown here illustrates the essence of the RTPIV method proposed in Equation 3-2: the RTPIV method enables a technique to balance the role of cross-correlation and that of the fundamental governing equation of COM by varying α. When a small α is used, the RTPIV method assigns more weight on the cross-correlation and approaches traditional TPIV. As the value of α increase, the method assigns more weight on the COM governing equation to complement the information provided by the cross-correlation.

Accompanying Figure 3-4a, Figure 3-4b shows the corresponding e_V obtained under different values of α used. First, it can be seen that when α was small enough (smaller than ~10^{-5}), the error remained constant at 10% as highlighted by the horizontal green dashed line. As mentioned earlier, the reason was that when α is small enough, the RTPIV method became essentially equivalent to traditional TPIV. And indeed, an e_V of ~10% represents a typical error the current unregularized TPIV method based on recent quantification efforts [8, 19, 71]. Then Figure 3-4b also shows that as the value of α gradually increased, e_V first decreased, then reached a minimal of 5.1% when $\alpha = 3 \times 10^{-4}$, and began to increase again. The fundamental reason behind such behavior was that as α increases, the RTPIV method attempted to balance the role of cross-correlation and that of the COM regularization. As Figure 3-4b shows, such balance was only optimal within a certain range of α (between ~0.1 and 10^{-5} in this case as highlighted by vertical green dashed lines). When α is too small (smaller than ~10^{-5} in this case), the role of regularization is negligible and the e_V will be just the same as unregularized TPIV. When α is too large (larger than ~0.1 in this case), the role of regularization is too large and not enough weight is assigned to the cross-correlation (i.e., the experimental data), and e_V will be larger than the unregularized TPIV.

Besides providing a further understanding of the RTPIV method, the above observations from Figure 3-4 also illustrate the importance, and the potential practical difficulty, of selecting α. In practice, the true velocity is unknown and therefore e_V is not available for selecting the optimal α in the way shown in Figure 3-4b. The plot shown in Figure 3-4b simply is not obtainable in practice. Therefore, significant past efforts have been invested to develop methods that depend only on quantities practically accessible to determine the optimal α [69]. This work adapted the so-called L-curve method [69], named after the overall L shape of the curve between of $\Sigma(-CC(V))$ versus $\Sigma|\nabla\cdot V|$, both quantities practically accessible. More specifically, the L-curve method searches for the optimal α in three steps. First, the regularized minimization problem as described in Equation 3-2 was solved by the RTPIV method multiple times at different α's, and then the $\Sigma(-CC(V))$ and $\Sigma|\nabla\cdot V|$ obtained under each α were recorded. Second, the $\Sigma(-CC(V))$ and $\Sigma|\nabla\cdot V|$ obtained in step 1 under different α's were plotted, providing the L-curve shown in Figure 3-4a. Third, the corner of the L-curve was located by finding the maximum curvature of the curve, and the corresponding α at the corner was taken as the optimal α. Conceptually, the L-curve method is based on two recognitions. First, the α corresponding to the corner of the L-curve, where its curvature peaks, represents an optimal balance between the contributions from the regularization (i.e., the $\Sigma|\nabla\cdot V|$ term) and the measurements (i.e., the $\Sigma(-CC(V))$ term). A different α would result in a sub-optimal tradeoff between the regularization and measurements because the trade-off is moving away from the point with maximum curvature. The second recognition is that e_V is insensitive to the selection of α around the corner. So that in practice, the L-curve method can still be effective even though the "corner" of the L-curve cannot be accurately identified due to either measurement or computation uncertainties.

With the L-curve method, the optimal α was determined to be 3×10^{-4} for the experimental translation data shown in Figure 3-3a and 3-3b. The corresponding corner is highlighted by the red square on the L-curve in Figure 3-4a. The effectiveness of the L-curve method was confirmed by the fact that the minimal e_V indeed occurred near α of

3×10^{-4} as shown in Figure 3-4b. The data shown in Figure 3-4 also illustrate the insensitivity of e_V with respect to α as aforementioned. The two blue squares in Figure 3-4a show the cases from two other values of α, 5×10^{-4} and 1.6×10^{-4}, one larger and one smaller than the optimal value picked by the L-curved method. As seen, the portion of the curve within these two values was wide enough to contain the entire "corner" region of the L-curve. As seen from Figure 3-4b, any value from this region can reduce e_V sufficiently close to the minimal level of ~5.1%.

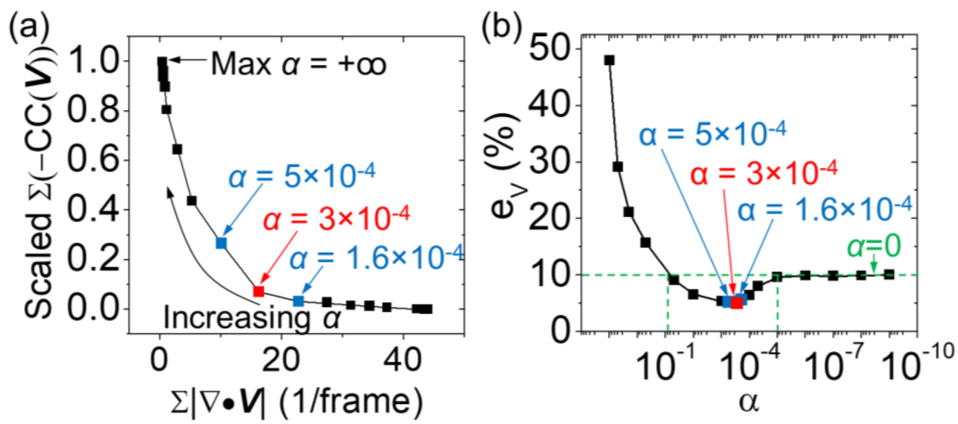

Figure 3-4 The L curve for the RTPIV method when applied to the controlled translation experiment. (a) The relationship between Σ(-CC(V)) and Σ|∇·V| with α varying from 0 to +∞. (b) Corresponding e_V at different values of α.

Figure 3-5 shows the validation results for the RTPIV method using the controlled rotation movement. As aforementioned, the experiment was similar to that of the translational movement described in Figure 3-3 and 3-4, except this time the solid samples were rotated. Two sets of projections were then captured at two consecutive positions of the rotation. Based on these projections, the RTPIV method was then applied to reconstruct the rotation field (with the same computational settings, e.g., voxel discretization and projection size, as used before). Figure 3-5a shows the 3D3C velocity vector distribution of the rotation movement obtained by the RTPIV method. As seen, the reconstruction faithfully captured the overall structure of the velocity field, i.e., a rotational field around the geometric center of the rotation. Quantitative examination was then performed by comparing the reconstruction against the ground truth. The e_V and e_D from the RTPIV method, averaged across the entire measurement domain, was calculated to be 6.2% and 1.1°. In comparison, when unregularized TPIV technique was applied using the same projections, e_V and e_D were 11.3% and 1.9°, respectively. The RTPIV method was again demonstrated to enhance measurement accuracy significantly.

Figure 3-5b and 3-5c show the velocity vector distributions at the central *z* plane (z = 6 mm) obtained by the RTPIV and TPIV method, respectively, to provide a visualization of the reconstructions. And Figure 3-5d shows the ground truth at the same plane. As can be seen from Figure 3-5b to 3-5d, the velocity field at central *z* plane obtained by RTPIV resembled the ground truth velocity field more closely than that acquired by TPIV.

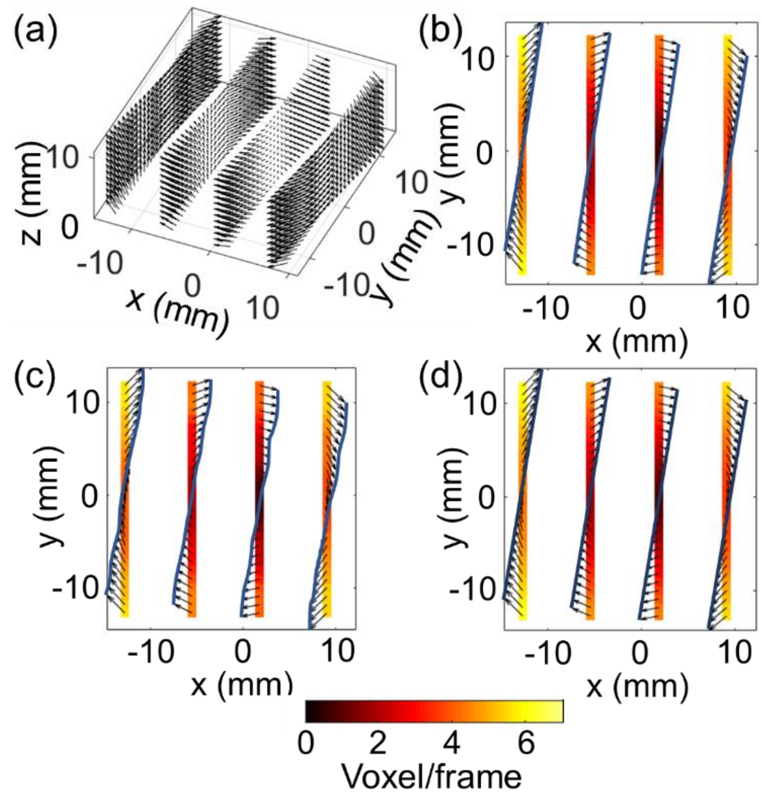

Figure 3-5 Comparison of the RTPIV and TPIV methods using the controlled rotation experiment. (a) Velocity vector distribution of the reconstructed rotation field obtained from RTPIV. (b) Reconstructed rotation field from RTPIV at the central z plane (z = 6 mm). (c) Reconstructed rotation field from TPIV at the same central z plane. (d) Ground truth rotation field at the same central z plane.

Similar to the controlled translation experiment, Figure 3-6 shows more intermediate steps and also illustrates the selection of α using the L-curve method. Figure 3-6a shows the scaled $\Sigma(-CC(V))$ versus $\Sigma|\nabla\cdot V|$ at various α. As can be seen, the result again followed the L shape, similar to that shown in Figure 3-4a for the controlled translation experiment. Figure 3-6b shows the corresponding e_V obtained at different values of α used. These results suggest the same key observations made from Figure 3-4b. The L shape seen in Figure 3-6a again reflected RTPIV's capability of balancing the cross-correlation and COM by varying α as formulated in Equation 3-2. From Figure 3-6b, it can be seen that when α was smaller than ~10^{-6}, the RTPIV method was essentially reduced to the unregularized TPIV method, with e_V =11.3% as highlighted by the horizontal green dashed line. Then as α increased, e_V first declined to a minimum of 6.2% at $\alpha = 1 \times 10^{-4}$, then started to increase again. When α increased beyond ~0.02, e_V obtained by RTPIV became larger than 11.3%.

Figure 3-6 also illustrates the selection of optimal α using the L-curve method. The L-curve, when applied to the data shown in Figure 3-6a, led to an optimal α =1×10^{-4}. The effectiveness of the L-curve method was again demonstrated by the corresponding e_V shown in Figure 3-6b. As shown, the minimal e_V indeed occurred in the vicinity of α =1×10^{-4}. Moreover, Figure 3-6 again illustrates that e_V was insensitive to the selection of α around the corner of the L curve. As seen from Figure 3-6a, with any α ranging from 2×10^{-4} and 5×10^{-5}, which covered essentially the entire "corner" region of the curve, the e_V obtained was sufficiently close to the minimal level of ~6.2% shown in Figure 3-6b.

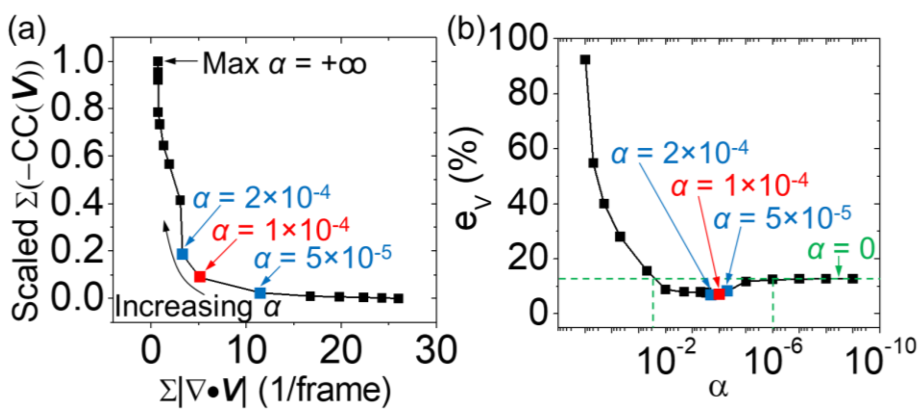

Figure 3-6 The L curve for the RTPIV method when applied to the controlled rotation experiment. (a) $\Sigma(-CC(V))$ versus $\Sigma|\nabla\cdot V|$ with α within $[0, +\infty]$. (b) e_V at different α's.

After the above validation of the RTPIV method using controlled experiments, numerical analyses were performed using more practical velocity fields. Numerical analyses were conducted here because for such practical fields, it was infeasible to obtain the ground truth velocity fields experimentally. Here, numerical analyses were performed on a jet flow and a pair of Rankine vortices so the effectiveness of the RTPIV method can be quantitatively evaluated on these canonical flows.

Figure 3-7 summarizes the results obtained from the jet flow simulations. The results of this jet flow were obtained via numerical simulations performed in the following four steps. First, the velocity vector field of a jet flow was obtained numerically by CFD simulations in Fluent. A volume of 14.4 × 14.4 × 4.8 mm^3 (along x, y and z directions, respectively) within the simulated field was created and then discretized into 240 × 240 × 80 voxels, inside of which a total of 24,000 numerical particles were randomly distributed spatially. Here these numerical particles were introduced to simulate the practical tracer particles seeded in the flow in the tomo-PIV experiment, and the spacing of these particles was ~0.4 mm on average, which was on the same order as that (i.e., ~0.5 mm) used in the above experiments. Secondly, the particles generated in step 1 were moved based on the local velocity vector of the jet flow. Third, two sets of six projections were calculated for the particles before and after the move in step 2. The projections were set to be at the same orientations as those used in the experiments (i.e., θ =219.5°, 270.0°, 315.7°, 50.1°, 118.6° and 139.0°). These calculations were conducted using a method combining ray-tracing and Monte Carlo simulations as detailed in our earlier work [52, 66]. To simulate major sources of practical measurement uncertainty, two types of artificial noises were added into the calculation of each projection, including a 1% background noise and a 0.3° VR error, following the suggestion from [19]. Fourth, the projections obtained in step 3 were fed into the RTPIV and TPIV methods separately to obtain the final velocity fields. The interrogation volume used in both methods was 32 × 32 × 32 voxels at 50% overlap, resulting in a 3D3C velocity field of 14 × 14 × 4 vectors.

Based on the above simulation approach, Figure 3-7a first shows the 3D3C velocity field of the jet flow reconstructed by the RTPIV method. Figure 3-7b and 3-7c then show the velocity vector distributions at the central z plane (z = 2.4 mm) extracted from the jet velocity fields obtained by RTPIV and TPIV, respectively. And Figure 3-7d shows the ground truth jet flow field (i.e., taken from the numerical solution) at the same central z plane. More specifically, the simulations were conducted for an air flow under a Reynolds number of 1.2×10^4 at jet exit (centered at x = 0 mm and y = -7.2 mm and issuing along the positive y direction). Based on these results, the e_V and e_D obtained by the RTPIV method were 4.5% and 1.1°, respectively. In comparison, the e_V and e_D were 9.1% and 1.7° obtained by the unregularized TPIV method. These error results agree with the observation on the velocity fields shown in Figure 3-7b ~ 3-7d: the velocity field obtained by RTPIV shown in Figure 3-7b resembled the ground truth field shown in Figure 3-7d more than that obtained by TPIV shown in Figure 3-7c. Therefore, the RTPIV method was able to significantly reduce the velocity error compared to the TPIV method, similar to the experimental results.

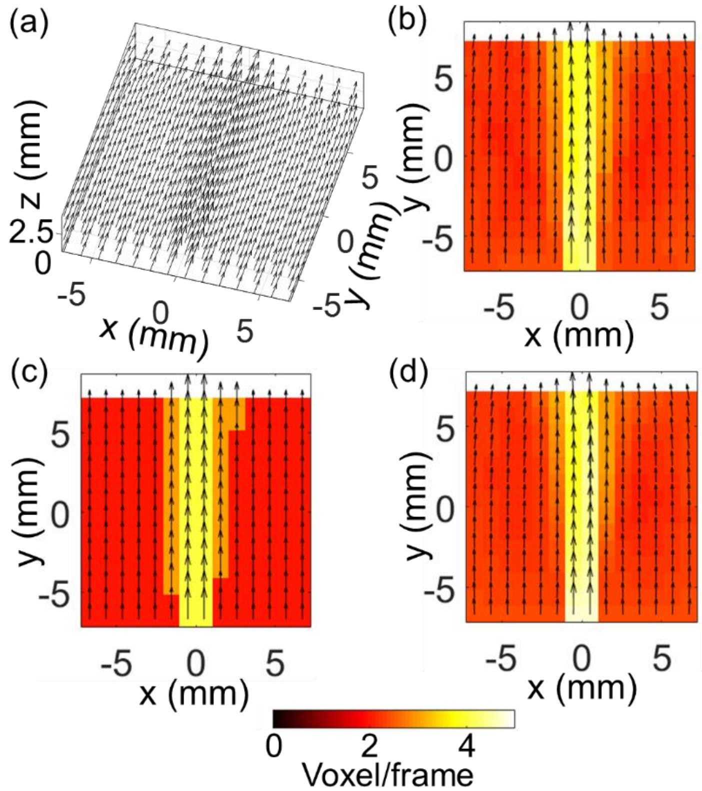

Figure 3-7 Comparison of the RTPIV and TPIV methods on a jet flow field. (a) Velocity vector distribution reconstructed by RTPIV. (b) Reconstructed field by RTPIV at the central *z* plane (*z* = 2.4 mm). (c) Velocity field reconstructed by TPIV at the same central *z* plane. (d) Ground truth jet flow field at the same central *z* plane.

Figure 3-8 summarizes the results from the numerical simulations of a pair of Rankine vortices, a more complicated flow field compared to the jet flow and also the controlled experiments. The results were obtained in the same steps as those used in Figure 3-7 with a few different parameters. First, the flow field was obtained using an analytical solution as detailed in [77] instead of CFD simulations. Second, the measurement volume was 48.0 × 36.0 × 9.6 mm^3, and the discretization was 800 × 600 × 160 voxels, in which a total of 400,000 numerical particles were seeded randomly. Third, an interrogation volume of 64 × 64 × 64 voxels at 50% overlap was employed in both RTPIV and TPIV methods to obtain a 3D3C velocity field of 24 × 17 × 4 vectors. With these modifications, Figure 3-8a first shows the 3D3C velocity field of the Rankine vortices reconstructed by the RTPIV method. Figure 3-8b and 3-8c then show the velocity vector distributions at central *z* plane (z = 4.8 mm) extracted from velocity fields of Rankine vortices obtained by RTPIV and TPIV, respectively. Figure 3-8d shows the ground truth velocity field of Rankine vortices at the same *z* plane. Comparing the reconstructed velocity field to its ground truth, the e_V and e_D for the RTPIV method were 6.6% and 1.4°, respectively, both substantially lower than 14.1% and 2.5° for the regularized TPIV method.

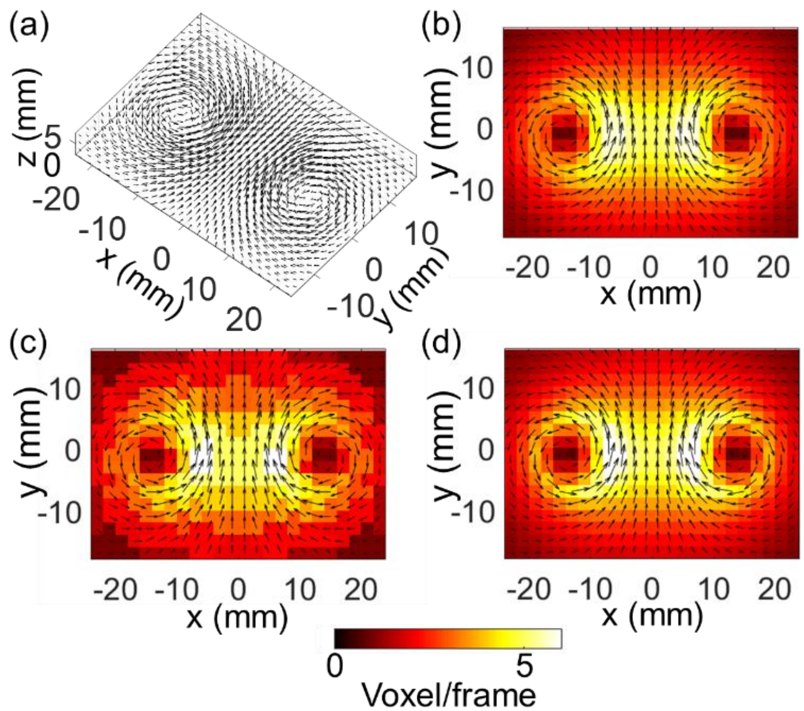

Figure 3-8 Comparison of the RTPIV and TPIV methods on a pair of Rankine vortices. (a) Velocity vector distribution reconstructed by RTPIV. (b) Reconstructed field by RTPIV at the central *z* plane (z = 4.8 mm). (c) Velocity field reconstructed by TPIV at the same central *z* plane. (d) Ground truth velocity field at the same central *z* plane.

Figure 3-9 and 3-10 provide the L-curves for results shown in Figure 3-7 and 3-8, respectively. Figure 3-9a first shows $\Sigma(-CC(V))$ versus $\Sigma|\nabla \cdot V|$ recorded from the jet flow simulations with α ranging from 0 to $+\infty$. As shown, Figure 3-9a again displays an approximate L shaped curve. Figure 3-9b shows the corresponding e_V obtained with varying α. Observations similar to the experimental results can be made from Figure 3-9b. When α is sufficiently small ($\alpha < 5 \times 10^{-6}$ in this case), the RTPIV method became equivalent to the unregularized TPIV method, which generated an error $e_V = 9.1\%$ as shown in Figure 3-9b. Then as α increased, e_V decreased to its minima 4.5% at $\alpha = 3 \times 10^{-4}$, the corner of the L-curve. With further increase beyond a certain level (7×10^{-2} in this case), e_V obtained by RTPIV began to exceed that of the unregularized TPIV method, leaving a relatively wide range of α (between 7×10^{-2} and 5×10^{-6}) where the RTPIV can outperform the unregularized method. In addition, Figure 3-9 again illustrates the insensitivity of e_V to the selection of α around the corner of the L-curve. With α ranging from 1×10^{-3} to 1×10^{-4}, as highlighted by blue squares both in Figure 3-9a and 3-9b, the e_V remained approximately around the minimal level of ~4.5%. Similar to Figure 3-9, Figure 3-10 shows the L-curve for the Rankine vortices. These results exhibit the same characteristics as those shown in Figure 3-9 and those obtained for the experimental results. One noteworthy observation is that in this case, the L-curve as shown in Figure 3-10 featured a more distinct "corner" than those seen earlier. A change of α from 1×10^{-3} to 5×10^{-5} corresponded to a relatively small region near this corner.

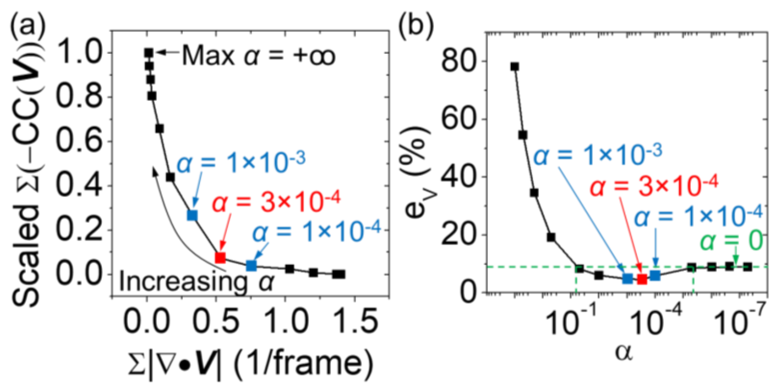

Figure 3-9 L-curve for the RTPIV method applied to a jet flow. (a) The relationship between Σ(-CC(V)) and Σ|∇·V| with α from 0 to +∞. (b) e_V with varying α.

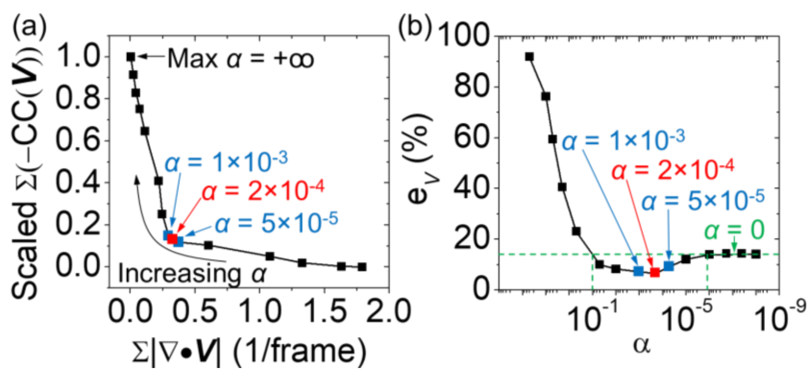

Figure 3-10 L-curve for the RTPIV method applied to a pair of Rankine vortices. (a) Σ(-CC(V)) versus Σ|∇·V| with α from 0 to +∞. (b) e_V at various α's.

Two notes are worth mentioning before leaving this section: one regarding noise-free simulations and the other about the computational time. First, a set of noise-free simulations were performed on the jet flow and Rankine vortices to further isolate the performance enhancement of the RTPIV compared to the TPIV method. These simulations were identical to the aforementioned simulations except one difference: this time without background noise or VR error added into the projection calculation. As a result, the RTPIV method was still able to improve the accuracy of velocity measurements by 35%~37% in terms of velocity magnitude and 0.4°~0.5° in terms of velocity orientation. Second, regarding the computational time, the accuracy enhancement of the RTPIV method comes at increased computational cost. For all the cases presented in this work, the RTPIV method consumed a total computational time of ~96 hours per case (36 hours on the reconstruction step and 60 hours on the regularized cross-correlation step) using a workstation with 16-Core Intel Xeon 2.6GHz and 512 GB memory, while the TPIV method consumed ~41 hours in contrast (36 hours on the reconstruction step and 5 hours on the cross-correlation step). As a result, the computational time required by the RTPIV method was ~2.3x of that of the TPIV method. Therefore, the application of the RPTIV method involves a consideration of whether the tradeoff between computational time and accuracy is feasible or worthwhile for a given application.

3.4 Summary

In summary, this work described the development and validation of a new method to reduce the uncertainties of 3D3C velocity measurements. The new method integrates regularization of the conservation of mass (COM) equation. This method enables improved accuracy by balancing the roles played by the measurements and the COM governing equation, so that the resulting 3D3C velocity field represents an optimal fit of both the experimental data and the governing equation. The new method was validated both experimentally (using controlled experiments) and computationally (using simulated canonical flows). The results demonstrated accuracy enhancement by 40~50% in terms of velocity magnitude and by 0.6~1.1° in terms of velocity orientation, compared to existing tomography PIV methods. Encouraged by these the validation results reported here, our ongoing work involves the application and assessment of the RPTIV method in realistic turbulent flows encountered in the experimental investigation of practical engineering devices/processes.

Chapter 4 Tomography reconstruction integrating view registration

Abstract

Tomographic measurements involve two steps: view registration (VR) to determine the orientation of the projections and the subsequent tomography reconstruction. Therefore, the practical error in both steps impacts the overall accuracy of the final tomographic measurements. Past work treated these two steps separately. This work shows that the overall tomography accuracy can be enhanced substantially if these two steps are considered holistically. Because there is an opportunity for each step to leverage the information in the other step to improve the overall accuracy if they are considered holistically. Based on this recognition, this work developed a new method (code named the RIVR method) to implement such a holistic scheme. The key of this implementation involved the use of the Metropolis criterion to adjust the initial orientation provided by traditional VR process dynamically. Both controlled experiments and accompanying numerical analyses were conducted to validate the RIVR method. Two sets of controlled experiments were conducted and analyzed, including a static uniform dye solution and turbulent flows, where the RIVR technique was demonstrated to significantly reduce the overall reconstruction error (by ~37% and ~35%, respectively) compared to past methods that treated VR and tomography separately.

4.1 Introduction

Tomography has been demonstrated as an effective diagnostic technique across a variety of applications, including medical imaging [78], electrical capacitance measurements [79], and also combustion and flow measurements [64, 80-83]. This work is performed under the context of combustion and flow measurements where tomography is used to obtain measurements that can resolve the three-dimensional (3D) spatial structure of key flow and flame properties with adequate temporal resolution [19, 72, 84-90]. A typical flow/flame tomography measurement consists of two steps. The first step uses multiple digital cameras placed at different locations and angular orientations to capture projection measurements of a target flow or flame property. The second step uses the projections captured in the first step as inputs for a tomography algorithm to reconstruct the 3D structure of the target property. A key process involved in the first step is view registration (VR), a process to determine the locations and orientations of the cameras, as the accuracy of the subsequent tomography reconstruction depends critically on the accuracy of the camera locations and orientations [22, 59, 64, 91, 92].

Accordingly, significant efforts have been invested in the VR process (step 1) and the tomography reconstruction algorithms (step 2), and have led to significant advancement in both. The investigation on the VR process focused on the development of better VR procedures and algorithms so that the camera locations and orientations can be determined with enhanced accuracy. Researchers examined a range of aspects, both experimental and computational, that can impact and improve the VR accuracy, including the use of different calibration targets (e.g., with a cylindrical shape [82, 92, 93] or a flat plate [45, 94-96]), the VR algorithms [97, 98], and effects caused by difficulty in the extraction of feature points due to the out-of-focus blurring inevitable in practice [99, 100]. In parallel to the investigation of the VR process, significant efforts have also been invested in the development of tomography reconstruction algorithms. Researchers in the flow and combustion community both adapted and modified algorithms established in other disciplines, and also developed new algorithms to either address or exploit the uniqueness features of flow and flame measurements. For example, the well-established ART and MART (algebraic reconstruction technique and multiplicative algebraic reconstruction technique) algorithms have been demonstrated to work effectively on combustion and flow problems [22, 82, 101]. Also, new algorithms and methods have been developed to either address or exploit unique aspects of flow and flames, such as the integration of *a prior* information [102, 103], the use of minimization algorithms to solve problems with limited views [67] and to exploit multi-spectral information [104], and the development of algorithms that can address nonlinearity (e.g., caused by strong absorption or radiation trapping) [72].

However, past efforts have treated the VR process (step 1) and the tomography reconstruction process (step 2) separately as two independent steps, even though these two steps are integral and their division is essentially arbitrary. Conceptually, it is intuitive to recognize that integrating both steps can potentially improve the overall tomography performance. Since both steps can only be performed with finite accuracy in practice, integration of them can enable a feedback mechanism between the VR and tomography process, so that each step leverages the information provided by the other to improve the its own accuracy. With this recognition, this work examined closely the benefits of integrating both steps in a holistic scheme, developed a corresponding method to implement the holistic scheme, and lastly demonstrated that it can indeed lead to significant improvement of the overall tomography performance both by numerical simulations and also by controlled experiments. The method that we developed to implement such a holistic concept is code named RIVR (reconstruction integration view registration). And the rest of the paper first details the mathematical background of the RIVR method, followed by its demonstration via both numerical simulations and controlled experiments.

4.2 Problem formulation and algorithm description

The mathematical formulation of 3D tomography has been previously detailed elsewhere [93, 105], and a brief summary is provided here to facilitate the discussion. The goal of 3D tomography is to measure the instantaneous 3D distribution of the target object (denoted as *F*) using multiple line of sight integrated projections (denoted as *P*) of *F* obtained by cameras (or other optical sensors) from different orientations. After proper discretization in the computational domain into voxels, the relationship between the measured *P* and the sought *F* is given by the following equation when the problem is a linear problem:

$$\boldsymbol{P} = \boldsymbol{PSF}\left(\theta,\phi,r\right)\cdot\boldsymbol{F} \tag{4-1}$$

where *P* represents the measured projections in a vector format by organizing the projections pixel by pixel, *F* the discretized target object also in vector format by organizing its values voxel by voxel, *PSF* the point spread function matrix that only depends on the geometry parameters of the imaging system used (i.e., not on *F*) [106]. Also note that this paper uses bold symbols to denote matrices and vectors, and normal symbols to denote scalars. The parameters of the imaging system include the distances and orientations of cameras relative to the target object, specified by θ (azimuth angle), ϕ (inclination angle), and r (distance) in a given coordinate system. Mathematically, the 3D tomographic problem is to solve for F with Ps measured at different locations and orientations specified by θ, ϕ, and r.

In practice, θ, ϕ and r were determined by a view registration (VR) process, so that the *PSF* matrix in Equation 4-1 can be computed before the tomographic problem can be solved. Due to various uncertainties encountered in practice, the VR process will only be able to determine θ, ϕ, and r within a certain level of error, and the error will propagate into the *PSF* matrix and the rest of the tomography process [19, 82], eventually manifested as an error in the reconstructed F. As an example, our past work was able to achieve an accuracy of 0.6° for the camera orientations (i.e., θ or ϕ) in the VR process [72, 107]. With this level of accuracy, when the VR and tomography reconstruction were performed separately, the resulting reconstruction error was in the range 7~11% approximately [72, 107].

As aforementioned, division of the problem formulated in Equation 4-1 into an independent VR process and a subsequent tomography process is essentially arbitrary and also unnecessary. Intuitively, integrating both steps can potentially improve the overall tomography performance by creating a feedback mechanism between the VR and tomography process and leveraging the information provided by each to improve the other. With this recognition, this work describes a new method, code named RIVR, to integrate both steps and solve the problem holistically.

The RIVR method was implemented in three steps. In the first step, a VR process was performed in the traditional way (e.g., following the process detailed in [45]) to obtain (θ, ϕ, r) to initialize the RIVR method. More specifically, the resulting (θ, ϕ, r) was used to compute the *PSF* using a ray-tracing method detailed in [52]. With the initial *PSF* obtained, the tomographic problem was solved to obtain F^i (where the superscript i stands for the initial solution of F). The projection formed by F^i was then computed (and denoted as P^i) using the same ray-tracing method detailed in [52].

The second step, the key step, adjusted the (θ, ϕ) provided by the initialization step with the information provided in the projections measured. As aforementioned, such adjustment was based on the recognition that (θ, ϕ) was noise contaminated and their accuracy could be improved by information provided in the measured projections. The adjustment was performed based on the difference (D) between P^i and P defined below,

$$D = \sum \left(\boldsymbol{P^i} - \boldsymbol{P} \right)^{\circ 2} \tag{4-2}$$

where the operator '∘2' represents the Hadamard square. In this second step, the orientation parameters (θ, ϕ) provided by the first step was perturbed by applying a random amount to form a new orientation (θ', ϕ'). The new orientation (θ', ϕ') was used to compute a new *PSF* and solve for a new F. Based on the new F, a set of new projections were computed and a new difference D (denoted as D') was determined. Then D' was compared to D by the Metropolis criterion [108] to decide if the current (θ', ϕ') should be rejected or accepted. If the decision was to reject, then the orientation parameters (θ, ϕ) provided by the first step was perturbed again to form another orientation (θ', ϕ'). If the decision was to accept, then the current (θ', ϕ') was regarded as a more accurate orientation for the cameras used, and be used as the starting point for the next round of perturbation. In this step, the use of the Metropolis criterion (the basis for stochastic optimization [108]) allowed the RIVR method to explore possible perturbations of (θ, ϕ) in all directions before deciding on the most promising direction, a key to enable the feedback between two complicated processes: the VR and tomography process.

The third and last step simply iterate step 2 until D converged, i.e., when the relative change in D between consecutive iterations became smaller than a preset level. In this work, the preset level was chosen to be 0.1% following the results in [68, 109]. Also, past work [72] has shown that the reconstruction accuracy was insensitive to this preset level (the reconstruction accuracy changed within 0.5% when the preset level varied between a range of 0.001% to 0.1%).

In summary, the above RIVR method integrated the VR and tomography process by establishing a feedback mechanism between them so that the end result is optimized holistically using information provided in both. Before leaving this section, note that the RIVR method requires more computational time than past practice (about 4x more time according to our testing) due to the iterative adjustment in step 2. Also note that here we only adjusted θ and ϕ, not r. The reason was that in our typical setup (where cameras are relatively far away from the target), the end result is significantly more sensitive to the uncertainty in the angular orientations (i.e., θ and ϕ) than to the distance (i.e., r). Therefore, the adjustment in r was not considered. In the application where r needs to be adjusted, the RIVR method can be straightforwardly extended.

4.3 Validation on a controlled dye solution

This section describes the experimental demonstration and validation of the proposed RIVR algorithm via controlled experiments, and the supporting numerical analysis. The setup for the controlled experiments is shown in Figure 4-1, and it was similar to that described in [96] and only a brief summary will be provided here. The major concept of the controlled experiments was the use of a well-mixed solution of Rhodamine 6G dye to create a uniform 3D distribution. The dye solution was excited by a laser volumetrically, and the laser induced fluorescence (LIF) signal emitted by the dye volumetrically (referred to as the VLIF signal hereafter) was collected by several cameras. Here LIF is a spectroscopic approach in which the target atoms or molecules are excited to a higher energy level by laser absorption followed by spontaneous emission [110]. Tomography reconstructions were then performed using the VLIF signals collected to obtain the 3D distribution of the dye concentration, which were then compared to the ground truth (i.e., the uniform distribution known *a prior*) to quantify the accuracy.

More specifically, the experimental setup consisted of three major components as shown in Figure 4-1: the dye solution, the laser, and the cameras. The dye solution was prepared by well mixing ethanol and Rhodamine 6G. This dye solution was contained in a cubical cell with a dimension of 50 mm × 50 mm × 50 mm, creating a precisely known concentration distribution. The dye solution was then illuminated volumetrically by a laser slab, generated by expanding the outputs from a pulsed Nd: YAG laser (Quanta-Ray Spectra-Physics, labeled as the VLIF laser shown in Figure 4-1). The LIF signals emitted by the dye were captured simultaneously by a total of 5 cameras (4 Photron SA4s and 1 SA6) at different positions and orientations as shown. These cameras were carefully aligned in the horizontal plane within experimental accuracy so that their orientations were completely specified by θ (defined as the angle formed by the optical axis of a given camera relative to the opposite propagation direction of the laser slab as shown). To facilitate the description of camera orientations and the following discussion, a right-handed Cartesian coordinate system was defined as shown in Figure 4-1: the origin O was defined as the center point of the cubical cell, the X axis was defined along the opposite propagation direction of the VLIF laser slab (which propagated perpendicularly into the dye cell), and the Z axis was defined to be out of the horizontal plane. Prior to any measurement, a traditional VR process was performed to determine the initial orientations of cameras [45, 97], and the orientations of cameras 1 through 5 were determined to be θ = 270.0°, 311.8°, 341.9°, 73.7° and 111.1°, respectively, with an error estimated to be ~0.6°.

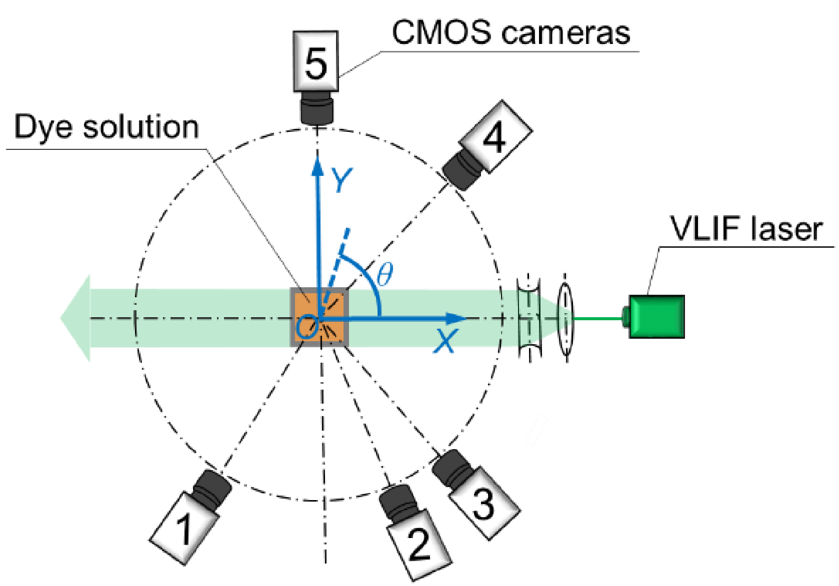

Figure 4-1 Setup of the validation experiments using a dye solution.

The validation experiments started with characterizing the incident VLIF laser slab intensity profile, because the subsequent tomography reconstruction algorithm needed the laser profile as an input to decouple the laser intensity variation from the dye absorption [72], and the resulting intensity profile of the laser slab used here was depicted in Figure 4-2a. The details to decouple the laser intensity from dye absorption were provided in [72], and are only summarized briefly here. The key concept involved in the decoupling was a nonlinear point spread function (NPSF). The NPSF extends the standard point spread function to accommodate laser attenuation during propagation (e.g., due to dye absorption) [72]. With the problem domain (i.e., the dye solution in this work) discretized into thin layers perpendicular to the laser propagation direction, the NPSF was applied iteratively layer by layer to decouple the laser intensity profile from the dye absorption.

After the above preparation, VLIF measurements were performed with all 5 cameras, and Figure 4-2b shows an example projection of VLIF signal captured by camera 5, as an illustration of the nature of the inputs fed into the tomography reconstruction. The pixel resolution of the projection was 800 × 800 and each pixel corresponded to a physical size of 0.05 mm × 0.05 mm. As seen in Figure 4-2b, the VLIF signals captured were not uniform even though the concentration of the dye was uniform. Because the VLIF signals depended both on the dye concentration and the local laser intensity profile, necessitating the characterization of the laser slab intensity described above. Based on the measured VLIF projections (and also the initial camera orientations from the VR process), the RIVR algorithm was used to obtain reconstructions of the 3D dye concentration, which was then compared against the ground truth to quantify the accuracy.

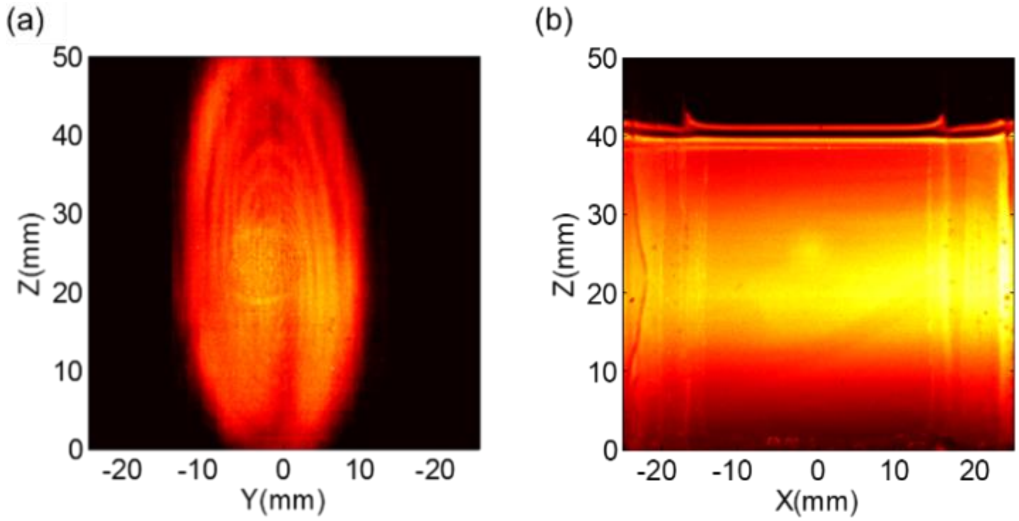

Figure 4-2 (a) VLIF laser slab intensity profile at X = 25 mm. (b) Projection captured by camera 5 for the controlled dye solution.

In the reconstruction, the computational domain was set to be a volume of 40 mm × 40 mm × 40 mm centered around the origin O, which was smaller than the volume of the dye cell to exclude non-ideal effect around the edges and corners of the cell. This computational domain was then discretized into 120 × 120 × 120 voxels, resulting in a voxel size of 0.33 mm in all three directions. The tomography algorithm used in the RIVR algorithm was an established method detailed in [72], and code named IRT (iterative reconstruction technique). It obtained the reconstruction iteratively by using the projections measured from different orientations at a time to refine it. Figure 4-3a shows a rendering of the reconstructed concentration across four planes (at X = 0 mm, Z = 10 mm, 20 mm and 30 mm) obtained by the RIVR algorithm, visually illustrating that the reconstruction reproduced the expected uniform distribution. To quantitatively assess the reconstruction performance, the following reconstruction error (e_R) was defined:

$$e_R = \frac{\sum \left| \boldsymbol{F}^{rec} - \boldsymbol{F}^{true} \right|}{\sum \boldsymbol{F}^{true}} \tag{4-3}$$

where F^{rec} and F^{true} represent the reconstructed and true concentration distributions, respectively. With this definition, the e_R for the reconstruction shown in Figure 4-3a over the entire computational domain was calculated to be 2.66%. To further examine the reconstruction accuracy, Figure 4-3b shows the concentration reconstructed by RIVR along three lines (Z = 10 mm, 20 mm, and 30 mm on the Y = 0 mm plane) together with the e_R along these lines. As shown, the RIVR algorithm was able to reconstruct the uniform concentration with e_R of 2.87%, 3.14%, and 2.97% at these locations.

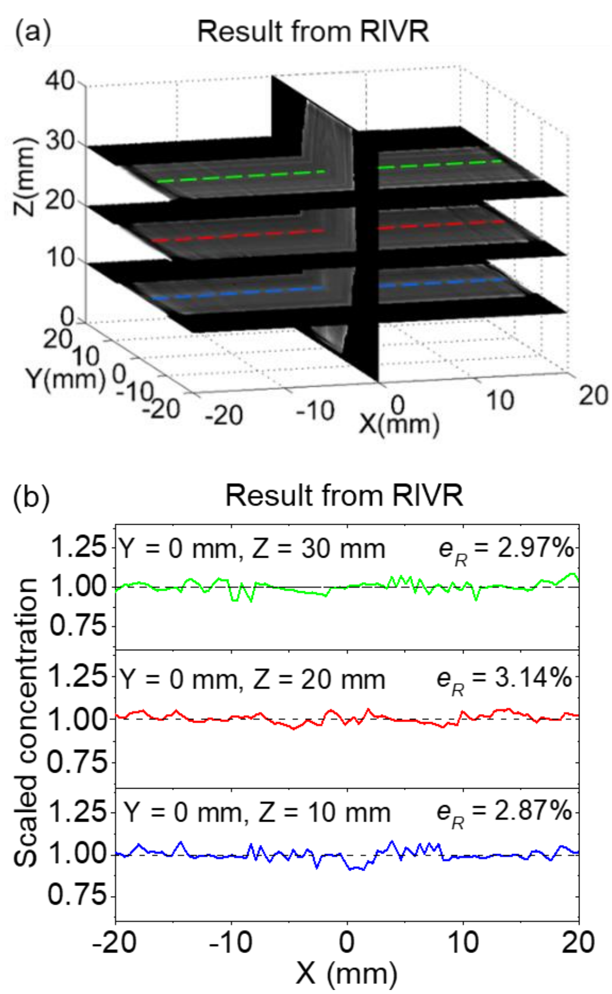

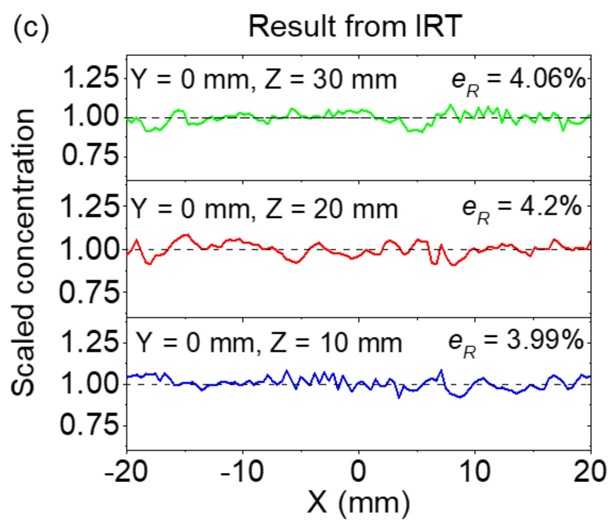

Figure 4-3 Comparison of the RIVR and IRT methods using controlled validation experiments. (a) Reconstructed concentration by RIVR at 4 selected planes (X = 0 mm, Z = 10, 20 and 30 mm). (b) Reconstructed concentration by RIVR along 3 lines with corresponding e_R. (c) Reconstructed concentration by IRT along 3 lines with corresponding e_R.

To illustrate the advantage of the RIVR algorithm, reconstruction of the same experimental data was also processed with the traditional method, where the VR and tomography were performed as two separate steps. More specifically in this case, the same cameras orientations obtained with the VR process and the measured projections as those used in the RIVR algorithm were fed into the same IRT algorithm. The only difference was that this time, the orientations were kept constant in the IRT algorithm. The e_R for the reconstruction obtained by the IRT method was calculated to be 4.20%, significantly higher than the 2.66% accuracy provided by the RIVR method (by ~37%). For closer examination, Figure 4-3c shows results from the IRT algorithm at the same three lines as in Figure 4-3b, together with their corresponding e_R (3.99%, 4.20% and 4.06%). As can be seen from Figure 4-3b and 4-3c, due to the more accurate reconstruction enabled by the RIVR method, the reconstructed concentration followed the actual uniform distribution more closely. Also note that at these 3 particular lines picked, the reconstruction errors were all larger than the error in the entire domain for the RIVR algorithm, and those for the IRT method were either at or smaller than that in the entire domain. Therefore, the e_R enhancement from the RIVR method were in general more dramatic than those shown in Figure 4-3b and 4-3c.

As mentioned in section 2, such superior performance from the RIVR method was brought about by establishing a feedback mechanism between the VR and tomography step, because this was the only difference between the RIVR and IRT methods applied above. As a demonstration of the feedback mechanism, the RIVR method was able to adjust the camera orientation to 271.1°, 311.6°, 341.1°, 73.8° and 111.7° for camera 1-5, respectively. Compared to the orientations determined by the VR process, the RIVR method adjusted them by 1.1°, -0.2°, -0.8°, 0.1° and 0.6°, respectively (in contrast, the traditional IRT method just used the orientations from the VR process as they were). To further confirm the effectiveness of the feedback mechanism, numerical analysis was performed. Because numerical analysis provides ground truth for both the target distribution (which was precisely known in the above validation experiments) and also the camera orientations (which are difficult to known *a prior* experimentally), so that the effects of the orientation adjustments can be examined and quantified.

The numerical analysis was performed in the following four steps. First, a uniformly distributed concentration phantom was created to simulate the dye concentration in the cubical cell used in the aforementioned validation experiments. Second, projections from five orientations were generated based on the phantom created in the first step. To reproduce the conditions of the experiments, these five orientations were set to be the same as those obtained by the VR process in the experiments (i.e., θ = 270.0°, 311.8°, 341.9°, 73.7° and 111.1°, respectively, for cameras 1 through 5). To simulate the validation experiments, a total of 3.0% of Gaussian noise was artificially added to the projections following the suggestion from [72] to simulate noises (e.g., background noise, shot noise, camera uncertainty, et al), and a ±0.6° error was randomly added to the projections (corresponding to the obtainable VR accuracy in our experiments). Third, these projections together with the orientations described in step 2, both contaminated with noises, were fed into the RIVR algorithm to perform the reconstruction. Fourth, the same projections and orientations described in step 2 were also fed into the IRT algorithm to perform the reconstruction, and the results were compared against those from the RIVR algorithm. The e_R across the entire simulation domain was 2.55% from the RIVR method and 4.15% from the IRT method. The RIVR method was able to significantly reduce the reconstruction error compared to the traditional method similar to the experiments. The results in Figure 4-4 show more detailed comparison of the reconstructed concentration by these two methods at several locations. These results resemble the experimental results shown earlier, providing further support of the RIVR method. Here we wanted to emphasize that in this comparison, the RIVR method started with the same view registration results as those used in the IRT method, and was able to provide reconstructions with enhanced accuracy due to the feedback mechanism introduced.

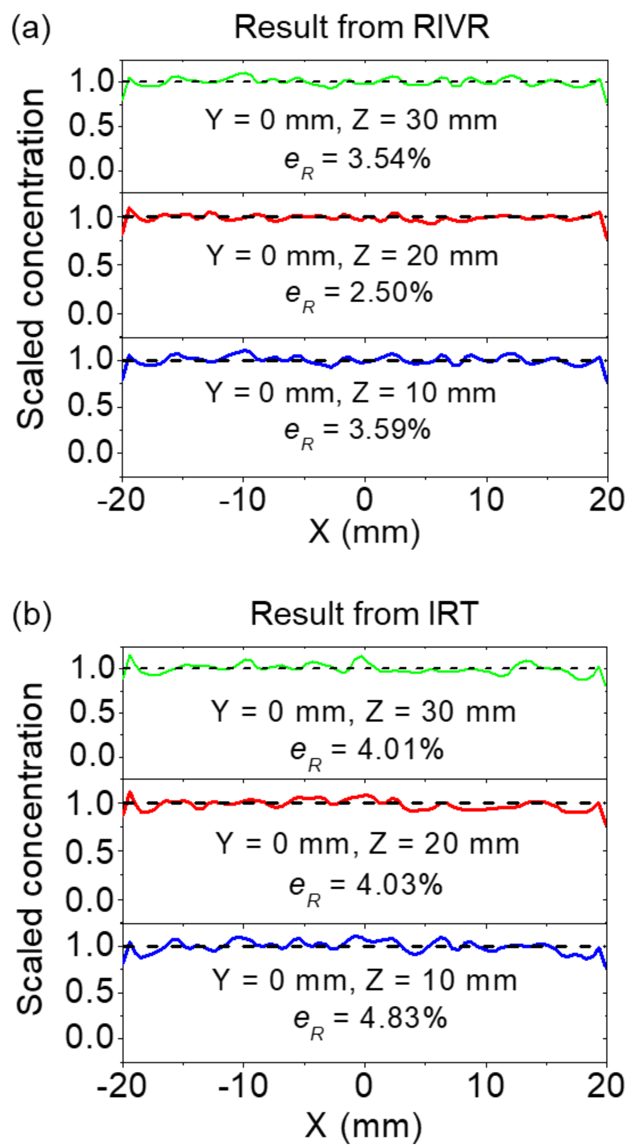

Figure 4-4 Comparison of the RIVR and IRT methods using numerical analysis. (a) Reconstructed concentration by RIVR along 3 lines with corresponding e_R. (b) Reconstructed concentration by IRT along 3 lines with corresponding e_R.

Figure 4-5 shows the orientation adjustments performed by the RIVR method and compares the orientations obtained vs the correct orientation, providing insights into the RIVR mechanism that cannot be easily obtained in experiments. Figure 4-5 compares the initial camera orientations fed into the RIVR algorithm and the optimized orientations obtained by the RIVR algorithm. The comparison was shown in terms of the error (denoted as $\Delta\theta$) of the initial and optimized orientations versus the correct orientation. As seen in Figure 4-5, the errors in the initial orientations were either 0.6° or -0.6° as mentioned earlier. And the RIVR method was able to optimize and reduce the orientations for four out of the five cameras used substantially from ±0.6° to 0.4°, 0°, 0.1°, and 0° (for cameras 1, 2, 3, and 5, respectively). As a result, the RIVR method was able to significantly reduce the overall reconstruction error as discussed earlier. Figure 4-6 further extends the comparison of the RIVR and IRT method under other levels VR accuracy with $\Delta\theta$ ranging from 0° to ±1.0°, while all the other settings (including the phantom, initial camera orientation set and gaussian noise level, etc.) remained the same as those used in the case with $\Delta\theta$ = ±0.6°. Note that the horizontal axis in Figure 4-6 means the range of the VR error, i.e., 1.0° on the horizontal axis means VR error is within ±1.0°. Figure 4-6 show several key observations. First, at $\Delta\theta$ = 0°, the RIVR and IRT method achieved the same level of reconstruction accuracy as they should intuitively. Because with completely accurate VR process, the RIVR and IRT method are completely equivalent. Secondly, RIVR was able to reduce e_R more dramatically compared to IRT when VR error becomes increasingly larger also as intuitively expected. As $\Delta\theta$ increases, traditional IRT performs reconstruction based on inputs with increasingly larger error and results in larger e_R. In contrast, RIVR enables the adjustment of camera orientations and compensates for the error, resulting in significantly reduced e_R compared to IRT. Third, the e_R obtained experimentally from RIVR or IRT was plotted at $\Delta\theta$ = 0.6° for both methods. And as seen, these experimental data points overlap with the simulations closely, providing a confirmation to the estimation ±0.6° as the VR accuracy achieved in the experiments.

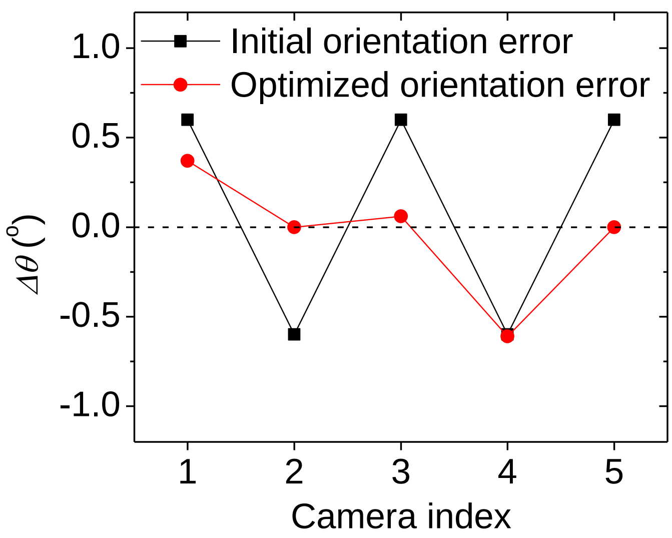

Figure 4-5 Comparison of initial camera orientations fed into the RIVR algorithm and the optimized orientation obtained by the RIVR algorithm.

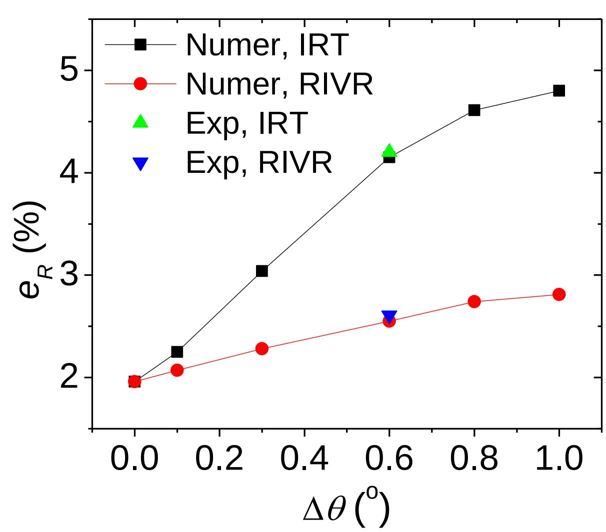

Figure 4-6 Comparison of reconstruction error obtained by RIVR and IRT under different VR errors.

Lastly, as a side note, the RIVR method is also observed to improve the convergence of the reconstruction in our work. As an example, Figure 4-7 compares the evolution of e_R in the RIVR and IRT methods as they iterated to reconstruct the results shown in Figure 4-4 and Figure 4-5. In the IRT method, e_R first decreased and reached a minimum near 4.2% at the 18th iteration, and then began to increase again as the iteration continues. Such a non-monotonic convergence has been observed for a variety of established reconstruction algorithms and is an important aspect of algorithm development [68]. In contrast, in the RIVR method, e_R decreased monotonically as it iterated as shown. To provide a limit for the convergence, the e_R that was achievable without zero VR error (i.e., $\Delta\theta = 0°$) was estimated to be about 2% in this case (determined by applying a few established algorithms and taking the minimum of their e_R). As seen, the RIVR method was able to converge monotonically towards this limit, and such monotonic convergence is a highly desirable feature for reconstruction algorithms.

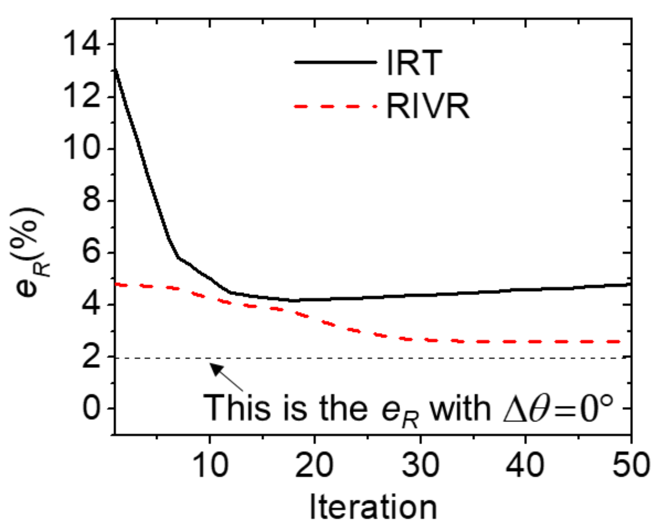

Figure 4-7 Convergence of e_R in the RIVR and IRT methods.

4.4 Application on turbulent flows

After the above validation with controlled experiments and numerical validations, this section reports an application of the RIVR algorithm on turbulent flows, with the goal of demonstrating the effectiveness of the RIVR method on 3D tomographic measurements in practical turbulent flows. The demonstration was based on the 3D tomographic imaging of a turbulent flow using VLIF signal from iodine (I_2) vapor seeded in the flow using an experimental setup shown in Figure 4-8. The experimental setup has been detailed else [96] and a brief summary is provided here.

This setup was largely similar as the controlled validation setup using the dye solution with two major differences. First, the dye solution was replaced by a turbulent flow. And second, a second laser was applied to simultaneously perform PLIF measurements so that accuracy of the 3D measurement can be quantified. The turbulent flow was formed by flowing nitrogen flow out of a nozzle with an exit diameter of 6.35 mm. At the exit of this nozzle, a rod with a diameter of 3.18 mm was placed to enhance turbulence and to create an easily recognizable V-shaped flow pattern to facilitate visual examination of the results. The flow was seeded with about 4% I_2 vapor by mole fraction. The seeded I_2 vapor was excited volumetrically to emit the VLIF signal, which were projected to 5 cameras as shown. The projections captured by these cameras provided the inputs to the subsequent tomographic reconstruction.

To provide a way to quantify the accuracy of the tomographic reconstruction, a planar measurement was taken simultaneously. The planar measurement involved a well-established PLIF technique based on I_2 vapor [110, 111]. As shown, a second laser (labelled the PLIF laser, Photonics Industries DM20-527DH) was used to generate the laser sheet for the PLIF measurement. The PLIF laser pulses were shaped by lenses into sheets with a thickness of ~0.8 mm, and then was aligned perpendicular to the optical axis of camera 1. Camera 1 was used to capture the PLIF signal. To better utilize the available cameras, camera 1 was configured in such a way that it captured the PLIF and VLIF signals sequentially in two consecutive frames with a time lag of 0.2 ms in between. The flow was essentially frozen during 0.2 ms considering the moderate turbulence levels in the target flow (with a Reynolds number of 2000 defined based on the jet exit diameter), therefore the 3D and PLIF measurements can be directly compared. Lastly, note that the coordinate system in this experiment was redefined as shown in Figure 4-8 to facilitate the remaining discussion: the origin *O* was defined as the center of the nozzle exit, *X* axis along the opposite direction of the PLIF laser propagation, and *Z* axis in the flow direction flow.

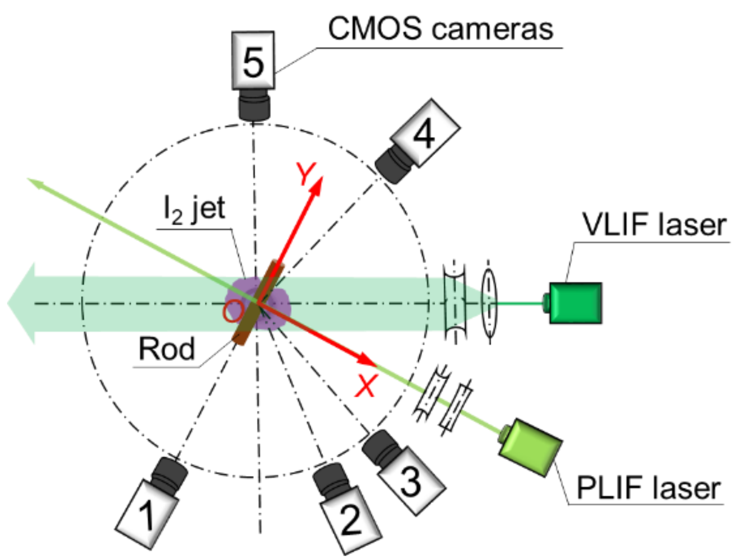

Figure 4-8 Demonstration of the RIVR method on turbulent flows measurements.

With the above setup, Figure 4-9a shows a set of example VLIF projections captured by camera 1 through 5 and the corresponding PLIF image captured by camera 1. Both the VLIF projections and the PLIF image display a turbulent jet flow with two branches formed by the rod placed at the exit of the nozzle as expected. All VLIF projections and the PLIF image had a resolution of 600 × 600 pixels, and each pixel corresponded to a physical size of 0.06 mm × 0.06 mm. Note that the PLIF image in Figure 4-9a appeared sharper than the VLIF projections as expected, due to the line-of-sight integrated nature of the VLIF projections.

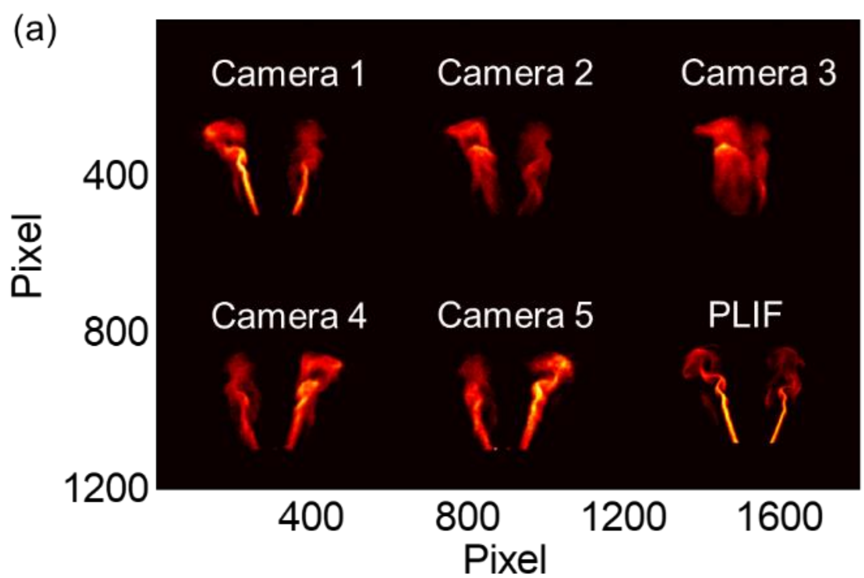

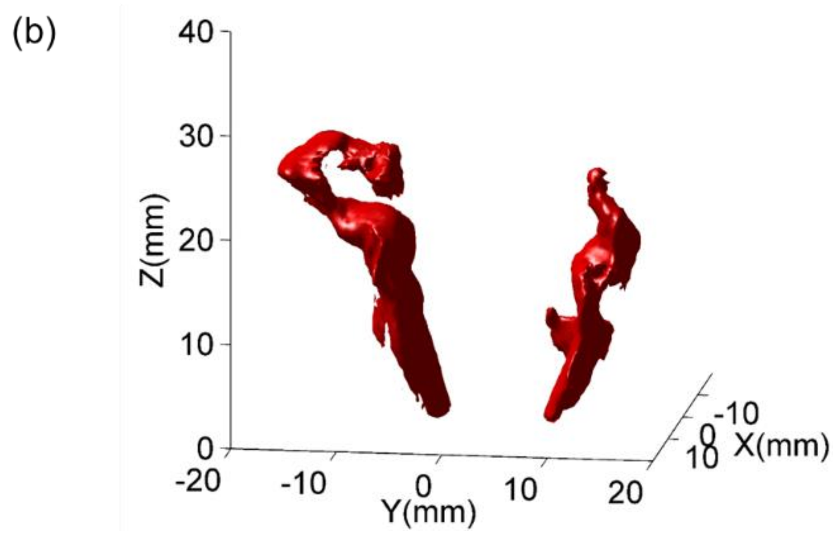

Figure 4-9 (a) A set of example VLIF projections captured by camera 1-5 and the PLIF image captured by camera 1. (b) 3D rendering of relative I_2 concentration reconstructed by the RIVR algorithm.

The RIVR method was then used to reconstruct the VLIF projections as those shown in Figure 4-9a together with the initial camera orientations obtained by the traditional VR method. The reconstruction was performed on a computational domain of 35.5 mm × 35.5 mm × 35.5 mm, discretized into 120 × 120 × 120 voxels, resulting in a voxel size of 0.30 mm in all three spatial directions. Figure 4-9b rendered the 3D I_2 concentration reconstructed by RIVR. Visual examination (e.g., by comparing Figure 4-9b to the VLIF projection captured by camera 1) suggests that the reconstruction captured the features of the V-shape flow. A quantitatively examination was then performed by comparing the RIVR reconstruction against the PLIF measurements as shown in Figure 4-10. Here, the concentration was also performed by the IRT method with the same VLIF projections. Figure 4-10a and 4-10b show the reconstruction obtained by RIVR and IRT at the central plane of the measurement domain (i.e., Y=0 mm), the location where the PLIF measurements were performed. Figure 4-10c and 4-10d compare the RIVR and IRT reconstructions against the PLIF measurement along three lines in this plane (i.e., Z = 18 mm, 15 mm and 12 mm within the Y = 0 mm plane as marked by the three dashed lines in Figure 4-10a and 4-10b). In these comparisons, due to the availability of the PLIF measurement, it was taken as the ground truth and used in Equation 4-3 for the calculation of the reconstruction error (e_R). From Figure 4-10c and 4-10d, it can be seen that, for the RIVR algorithm, e_R was 5.65%, 8.40% and 8.71% at Z = 12 mm, 15 mm, and 18 mm. In comparison, for the IRT method, e_R was 11.9%, 12.9% and 11.8%, significantly larger than that of the RIVR results. Across the entire central plane at Y = 0 mm, e_R was 7.03% and 11.3% for RIVR and IRT, respectively. Thus, the RIVR method was demonstrated to reduce the reconstruction error by ~38% than the traditional IRT method. In addition to the results shown here, this work also applied the RIVR technique on a variety of other turbulent flows measurements (a total of 8 different cases), and the error reduction were in a range of [31%, 42%] with an average of 35% compared to the traditional IRT technique. Therefore, the results shown here represented a case with average error reduction.

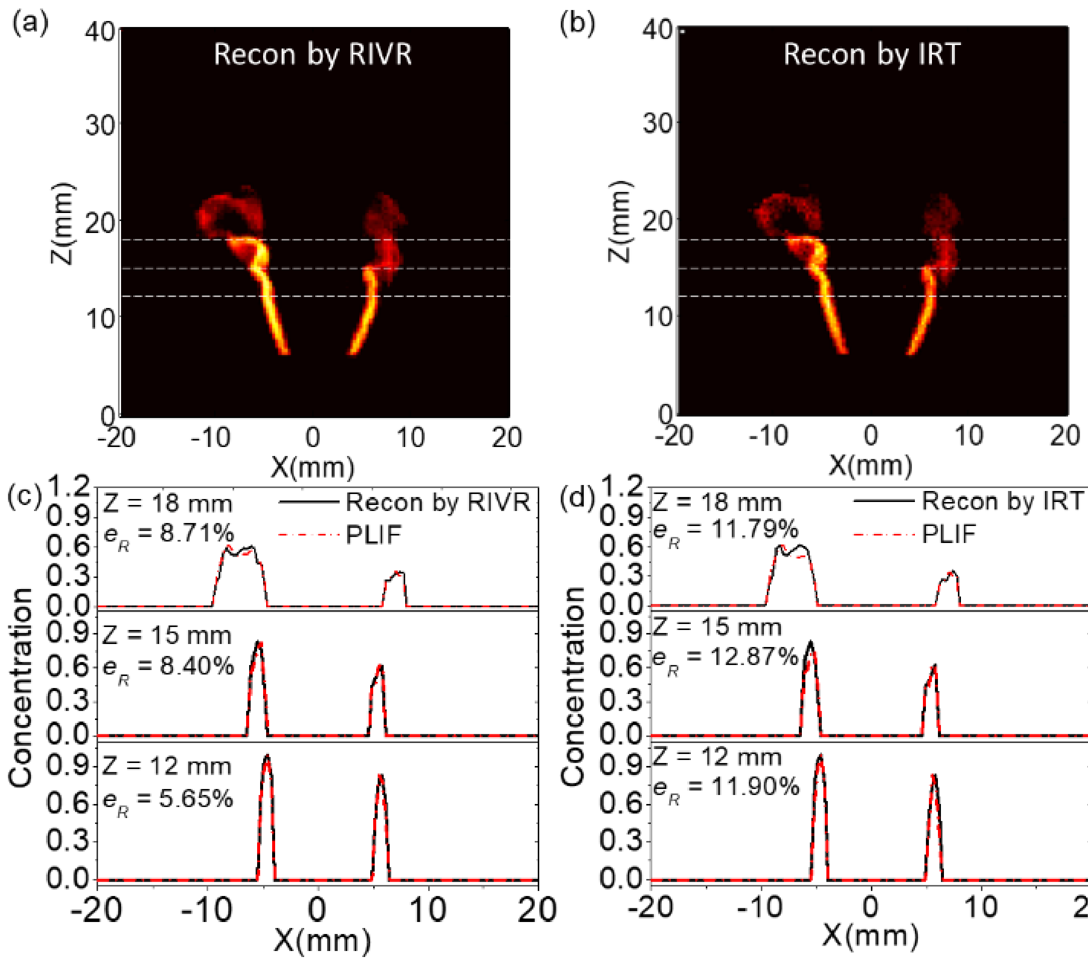

Figure 4-10 Comparison of the RIVR and IRT methods on turbulent flows. Panels (a) and (b): Reconstructed concentration across the central plane (Y = 0 mm) from RIVR and IRT, respectively. (c) Comparison between RIVR and PLIF along three lines (Z = 12 mm, 15 mm and 18 mm and Y = 0 mm as marked in Figure 4-10a. (d) Comparison between IRT and PLIF along the same lines as in panel (c).

As aforementioned, the above improvement was brought about by RIVR's ability to optimize the VR and tomography processes holistically. In the comparison shown in Figure 4-10, the RIVR method adjusted the camera orientations by 1.1°, -0.2°, -0.1°, 0.1°, and 0.6° for cameras 1 through 5, respectively. To further illustrate the effects of such adjustment, a numerical analysis similar to that performed on the controlled dye solution was conducted. Here again, the idea was to use simulations, in which both the target distribution and camera orientations were known *a priori*, to quantify the performance of the RIVR method. The numerical simulations here were entirely parallel to those performed on the controlled dye solution as detailed in Section 3 with one difference: the flow as shown in Figure 4-9b (i.e., reconstructed using experimentally measured projections shown in Figure 4-9a) was directly used as the numerical phantom now. The results were summarized in Figure 4-11 and 4-12.

Figure 4-11 shows that the RIVR method indeed was able to reduce the initial VR errors. More specifically, the RIVR method was able to reduce the initial VR error of $\Delta\theta$ = ±0.6° to 0.14° on average with almost 0.0° error for four out of the five cameras (cameras 1, 2, 4, and 5), and a slightly larger error of 0.7° (than 0.6°) for camera 3. Such slightly larger error of 0.7° for camera 3 was caused by the stochastic and global optimization nature of the RIVR method. As described in Section 2, the RIVR method uses the Metropolis criterion, a stochastic technique, to perform the optimization globally. Hence, the goal of the RIVR technique was not to reduce all the individual VR errors for each camera, but to reduce the global reconstruction error, as shown by the results (the averaged VR error was reduced from 0.6° to 0.14° and the overall reconstruction error by ~38%). Figure 4-12 repeats the comparison between the RIVR and IRT methods at different levels of VR error ranging from $\Delta\theta$=0.0° to ±1.0°. Similar to the results obtained earlier for the dye solution, the RIVR method outperformed IRT on all levels of $\Delta\theta$, and the outperformance became more dramatic as the VR error increases. Lastly, also note that at

$\Delta\theta$=±0.6°, the e_R from the numerical simulations was 6.40% for the RIVR method and 10.8% for the IRT, reasonably close to the experimental results (i.e., 7.03% and 11.3%, respectively) as shown.

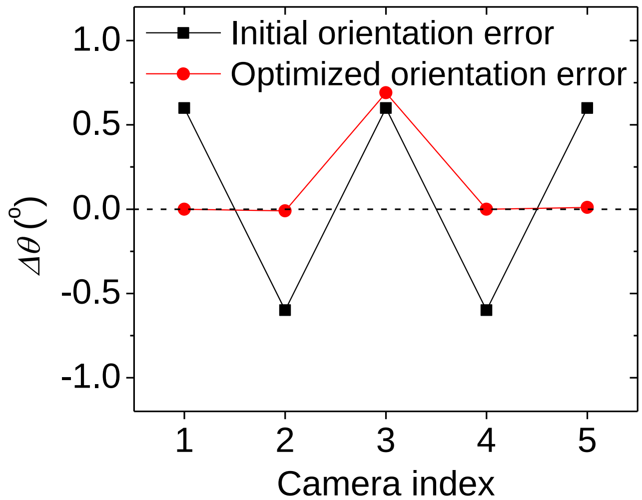

Figure 4-11 Comparison of initial camera orientations fed into the RIVR algorithm and the optimized orientation obtained by the RIVR algorithm in the turbulent flow cases.

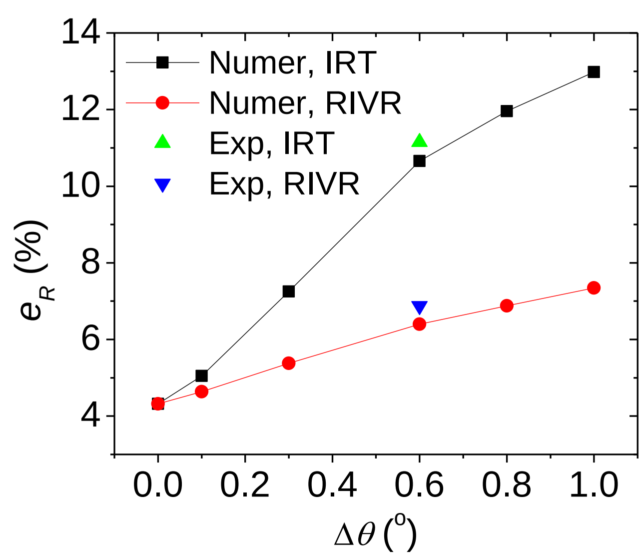

Figure 4-12 Comparison of the RIVR and IRT under different VR accuracy for turbulent flows.

4.5 Summary

In summary, this work reports the development and validation of a new tomography method (code named RIVR) for 3D measurements. Past methods treated view registration (VR) and tomography reconstruction as two separate steps. The new RIVR method was based on the recognition that integrating both steps can improve the overall tomography performance by enabling a feedback mechanism between the VR and tomography process. So that each step leverages the information provided by the other to improve the overall accuracy holistically. Based on this recognition, this work developed a method to implement such holistic scheme. The key of this implementation was the use of the Metropolis criterion to adjust the initial orientation provided by the traditional VR process iteratively and probabilistically. The RIVR method was validated both experimentally and numerically. The experimental validation involved creating controlled experiments based on a volumetric laser induced fluorescence technique, so that the performance of the new RIVR method can be compared quantitatively against established method. Two sets of controlled experiments were designed and conducted, including a static uniform solution and turbulent flows, where the RIVR technique was demonstrated to considerably reduce the overall reconstruction error (by ~37% and ~35%, respectively) compared to past methods that treated VR and tomography separately. Corresponding numerical analyses were performed to show that such enhanced reconstruction accuracy was enabled by the ability of the RIVR method to adjust view orientations holistically and reduce the error in the VR step.

Chapter 5 Conclusions and future work

5.1 Conclusions

In summary, this dissertation first reported an experimental quantification of the existing tomo-PIV uncertainty using controlled measurements, and then described the development and validation of two novel techniques, code-named RTPIV (Regularized Tomographic Particle Image Velocimetry) and RIVR (Reconstruction integrating View Registration), for improving the accuracy of 3D3C optical velocimetry. Conceptually, the RTPIV method improves the accuracy of 3D3C velocity measurements by incorporating the conservation of mass (COM) equation into the cross-correlation. The RIVR method enhances the accuracies of tomography and the resulting velocity by integrating tomography and VR and building a feedback connection in between. Both techniques have been validated experimentally using controlled experiments and numerically using phantom simulations. The results demonstrated that these techniques can indeed improve the accuracy of 3D3C velocimetry, and be expected to expand the application of tomographic PIV measurements when accurate and quantitative 3D flow properties are required.

More specifically, Chapter 2 first described an experimental quantification of tomo-PIV accuracy using controlled measurements which laid the ground work for the following developments of two novel techniques. The controlled measurements were designed by performing tomo-PIV measurements on a solid sample embedded with tracer particles, while the sample was moved both translationally and rotationally to create various known displacement fields. So that the 3D3C displacements measured by tomo-PIV can be directly compared to the known displacements created by the sample. The results illustrated that the tomo-PIV technique was able to reconstruct the 3D3C velocity with an averaged error of 0.8–1.4 voxels in terms of magnitude and 1.7°–1.9° in terms of orientation for the velocity fields tested. These results obtained from controlled tests aided the error analysis and developments of two novel tomo-PIV techniques (i.e., RTPIV and RIVR).

After recognizing the current tomo-PIV accuracy, Chapter 3 and 4 then presented RTPIV and RIVR to significantly enhance the accuracy of the tomo-PIV measurements. Chapter 3 first described the development and the validation of the RTPIV method, motivated by the need of tomo-PIV accuracy enhancement. The major idea of the RTPIV method is that it improves the accuracy of 3D3C velocity measurements by incorporating the conservation of mass (COM) equation as *a priori* information into the cross-correlation process. This RTPIV method was demonstrated and validated both experimentally and numerically. The results illustrated that the method was able to significantly enhance the accuracy of 3D3C velocity measurements, compared to the existing tomo-PIV technique.

Chapter 4 then described the development and the validation of the RIVR method, also motivated by the requirement of accuracy improvement of 3D tomography diagnostics. This RIVR method focuses on the tomography process, and it enhances the accuracies of tomography and the resulting velocity by integrating tomography and VR holistically. The accuracy enhancement can be achieved, because the integration of tomography and VR establishes a feedback connection between them and leverages the information provided by each step. Both controlled experiments and accompanying numerical analyses were conducted to validate the RIVR method. Two sets of controlled experiments were conducted and analyzed using a static uniform dye solution and turbulent flows, where the RIVR technique was demonstrated to significantly reduce the overall reconstruction error, compared to past methods that treated VR and tomography separately.

5.2 Future work

The above work can help to suggest three possible research directions for future work, as below:

1) The validation of the RTPIV technique on real flow measurements and its application of obtaining flow properties. First, the RTPIV technique needs to be validated experimentally on real flows. This dissertation developed the RTPIV technique and validated the RTPIV method using controlled motion experiments on solid samples embedded with particles. The controlled motions including a translation and a rotation are quite simple and ideal. In practice, real flows are much more complicated with flow structures (e.g., vortices) at various spatial and temporal scales, posing a challenge to the RTPIV technique. Second, the RTPIV method can be extended to obtain flow properties, such as strain, stress, and force. These properties are 3D in nature, and past work largely relied on the 2D PIV technique to estimate them or on the relatively low-accuracy tomo-PIV method to measure them. Therefore, direct 3D measurements of these flow properties with adequate accuracy have long been desired. Now, the recently developed RTPIV method is expected to enable such direct 3D measurements of these properties with an improved accuracy.

2) The completion of the RIVR technique on 3D3C velocity measurements. As a technique for velocimetry, the RIVR technique was developed to enable 3D3C velocity measurements with an improved accuracy. Nonetheless, the current version of RIVR has been developed and demonstrated only on 3D concentration measurements. The next step is to complete the development of the RIVR technique on 3D3C velocity measurements. One issue might pose a challenge to this development completion, and hence requires special attention: the computational cost of RIVR needs to be reduced when extending RIVR to 3D3C velocity measurements. As mentioned in Chapter 4, RIVR requires more computational time than past methods (about 4 times) to converge on a final 3D reconstruction. However, the typical particle reconstruction involved in the current 3D3C velocimetry is already computationally expensive (~2 days), due to the requirement of high-resolution reconstruction of small-scale particles. If we directly apply RIVR to the particle reconstruction in 3D3C velocimetry, the total computational cost will be combinatorically explosive, hindering RIVR's application in practical flow measurements. Thus, some extra adaptions of the current RIVR are required to reduce its computational cost, when extending RIVR to 3D3C velocimetry.

3) The extension of the RIVR technique to 3D LIF measurements of chemical radicals in reactive flows. First, it is interesting to examine whether RIVR can be effectively applied to 3D LIF measurements of chemical radicals in reactive flows. The LIF here is typically used to mark the key radicals (e.g., CH) in combustion studies. As a result of the turbulence-chemistry interaction, most radicals exist only in certain

regions (e.g., CH radicals exist in thin flame front layers). This results in a completely different spatial structure from the currently measured volumetric concentration of the tracers which exist everywhere within the flow domain. Second, it is also desired to quantify the final benefits that the RIVR method can bring about on key flame properties. The distributions of radicals can be used to infer key combustion and flame properties, such as flame surface density, which are inherently 3D. However, in the past, these properties were obtained using 2D measurements or relatively low-accuracy 3D measurements. As a high-accuracy 3D measurement technique, the RIVR application is expected to lead to key flame properties with adequate accuracy.

References

[1] R.J. Adrian, J. Westerweel, Particle image velocimetry, Cambridge University Press2011.

[2] M. Raffel, C.E. Willert, S. Wereley, J. Kompenhans, Particle image velocimetry: a practical guide, Springer2013.

[3] Y. Cheng, M. Torregrosa, A. Villegas, F. Diez, Time Resolved Scanning PIV measurements at fine scales in a turbulent jet, International Journal of Heat and Fluid Flow 32 (2011) 708-718.

[4] S. Burgmann, C. Brücker, W. Schröder, Scanning PIV measurements of a laminar separation bubble, Experiments in Fluids 41 (2006) 319-326.

[5] C. Brücker, D. Hess, J. Kitzhofer, Single-view volumetric PIV via high-resolution scanning, isotropic voxel restructuring and 3D least-squares matching (3D-LSM), Measurement Science and Technology 24 (2012) 024001.

[6] J. Zhang, B. Tao, J. Katz, Turbulent flow measurement in a square duct with hybrid holographic PIV, Experiments in Fluids 23 (1997) 373-381.

[7] K.D. Hinsch, Holographic particle image velocimetry, Measurement Science and Technology 13 (2002) R61.

[8] G.E. Elsinga, F. Scarano, B. Wieneke, B.W. van Oudheusden, Tomographic particle image velocimetry, Experiments in fluids 41 (2006) 933-947.

[9] F. Scarano, Tomographic PIV: principles and practice, Meas. Sci. Tech. 24 (2013) 012001.

[10] G.E. Elsinga, B. Wieneke, F. Scarano, A. Schröder, Tomographic 3D-PIV and applications, Particle image velocimetry, Springer2007, pp. 103-125.

[11] G. Elsinga, J. Westerweel, F. Scarano, M. Novara, On the velocity of ghost particles and the bias errors in Tomographic-PIV, Experiments in fluids 50 (2011) 825-838.

[12] S. Burgmann, W. Schröder, Investigation of the vortex induced unsteadiness of a separation bubble via time-resolved and scanning PIV measurements, Experiments in Fluids 45 (2008) 675.

[13] W. Zhang, R. Hain, C.J. Kähler, Scanning PIV investigation of the laminar separation bubble on a SD7003 airfoil, Experiments in Fluids 45 (2008) 725-743.

[14] J. Trolinger, Airborne holography techniques for particle field analysis, Annals of the New York Academy of Sciences 267 (1976) 448-459.

[15] A. Tonomura, Electron-holographic interference microscopy, Advances in Physics 41 (1992) 59-103.

[16] T. Hirayama, J. Chen, T. Tanji, A. Tonomura, Dynamic observation of magnetic domains by on-line real-time electron holography, Ultramicroscopy 54 (1994) 9-14.

[17] Q. Gao, H. Wang, G. Shen, Review on development of volumetric particle image velocimetry, Chinese science bulletin 58 (2013) 4541-4556.

[18] M.P. Arroyo, K.D. Hinsch, Recent developments of PIV towards 3D measurements, Particle image velocimetry, Springer2007, pp. 127-154.

[19] N. Liu, Y. Wu, L. Ma, Quantification of tomographic PIV uncertainty using controlled experimental measurements, Applied Optics 57 (2018) 420-427.

[20] B. Wieneke, PIV uncertainty quantification from correlation statistics, Measurement Science and Technology 26 (2015) 074002.

[21] D.R. Neal, A. Sciacchitano, B.L. Smith, F. Scarano, Collaborative framework for PIV uncertainty quantification: the experimental database, Measurement Science and Technology 26 (2015) 074003.

[22] F. Scarano, Tomographic PIV: principles and practice, Measurement Science and Technology 24 (2012) 012001.

[23] W. Xu, N. Liu, L. Ma, Super resolution PLIF demonstrated in turbulent jet flows seeded with I2, Optics & Laser Technology 101 (2018) 216-222.

[24] R. Hain, C.J. Kähler, D. Michaelis, Tomographic and time resolved PIV measurements on a finite cylinder mounted on a flat plate, Experiments in Fluids 45 (2008) 715-724.

[25] A. Schröder, R. Geisler, G.E. Elsinga, F. Scarano, U. Dierksheide, Investigation of a turbulent spot and a tripped turbulent boundary layer flow using time-resolved tomographic PIV, Experiments in Fluids 44 (2008) 305-316.

[26] J. Weinkauff, D. Michaelis, A. Dreizler, B. Böhm, Tomographic PIV measurements in a turbulent lifted jet flame, Experiments in Fluids 54 (2013) 1624.

[27] E. Baum, B. Peterson, C. Surmann, D. Michaelis, B. Böhm, A. Dreizler, Investigation of the 3D flow field in an IC engine using tomographic PIV, Proceedings of the Combustion Institute 34 (2013) 2903-2910.

[28] B. Wieneke, Volume self-calibration for 3D particle image velocimetry, Experiments in fluids 45 (2008) 549-556.

[29] N. Liu, Q. Lei, Y. Wu, L. Ma, 3D tomography reconstruction improved by integrating view registration, Applied Optics 58 (2019) 2596-2604.

[30] N. Liu, L. Ma. 3D Flame Measurements Using Tomography Reconstruction Integrating View Registration. In: AIAA Scitech 2020 Forum; 2020. p. 2208.

[31] D. Michaelis, M. Novara, F. Scarano, B. Wieneke. Comparison of volume reconstruction techniques at different particle densities. In: 15th International Symposium on Applications of Laser Techniques to Fluid Mechanics; 2010; Lisbon, Portugal. p. 3-17.

[32] M. Novara, F. Scarano, Performances of motion tracking enhanced Tomo-PIV on turbulent shear flows, Experiments in Fluids 52 (2012) 1027-1041.

[33] S. Discetti, T. Astarita, A fast multi-resolution approach to tomographic PIV, Experiments in Fluids 52 (2012) 765-777.

[34] S. Petra, C. Schnörr, A. Schröder, B. Wieneke, Tomographic image reconstruction in experimental fluid dynamics: synopsis and problems, Mathematical Modelling of Environmental and Life Sciences Problems, (2007) 1-21.

[35] S. Petra, A. Schröder, C. Schnörr, 3D tomography from few projections in experimental fluid dynamics, Imaging Measurement Methods for Flow Analysis, Springer2009, pp. 63-72.

[36] X. Li, L. Ma, Minimizing binary functions with simulated annealing algorithm with applications to binary tomography, Computer Physics Communications 183 (2012) 309-315.

[37] S. Gesemann, D. Schanz, A. Schröder, S. Petra, C. Schnörr, Recasting tomo-piv reconstruction as constrained and l1-regularized non-linear least squares problem, 15th

International Symposium on Application Laser Techniques to Fluid Mechanics, Lisbon, Portugal, 2010, pp. 1-12.

[38] M. Novara, A. Ianiro, F. Scarano, Adaptive interrogation for 3D-PIV, Measurement Science and Technology 24 (2012) 024012.

[39] F. Schrijer, F. Scarano, Effect of predictor–corrector filtering on the stability and spatial resolution of iterative PIV interrogation, Experiments in Fluids 45 (2008) 927-941.

[40] N. Liu, L. Ma, Regularized tomographic PIV for incompressible flows based on conservation of mass, Applied Optics 59 (2020) 1667-1677.

[41] C. De Silva, R. Baidya, M. Khashehchi, I. Marusic, Assessment of tomographic PIV in wall-bounded turbulence using direct numerical simulation data, Experiments in fluids 52 (2012) 425-440.

[42] K.P. Lynch, F. Scarano, Experimental determination of tomographic PIV accuracy by a 12-camera system, Measurement Science and Technology 25 (2014) 084003.

[43] M. Kang, X. Li, L. Ma. Calibration of Fiber Bundles for Flow and Combustion Measurements. In: AIAA Paper (2014-0397); 2014; National Harbor, MD. p.

[44] J.Y. Bouguet, Complete camera calibration toolbox for matlab. 2002.

[45] M. Kang, Y. Wu, L. Ma, Fiber-Based Endoscopes for 3D Combustion Measurements:View Registration and Spatial Resolution, Combust. Flame 16 (2014) 3063–3072.

[46] Q. Lei, Y. Wu, H. Xiao, L. Ma, Analysis of four-dimensional Mie imaging using fiber-based endoscopes, Appl. Opt. 53 (2014) 6389-6398.

[47] P. Sahoo, C. Wilkins, J. Yeager, Threshold selection using Renyi's entropy, Pattern recognition 30 (1997) 71-84.

[48] R.J. Adrian, Twenty years of particle image velocimetry, Experiments in Fluids 39 (2005) 159-169.

[49] C.E. Willert, M. Gharib, Digital particle image velocimetry, Experiments in Fluids 10 (1991) 181-193.

[50] C. Atkinson, J. Soria, An efficient simultaneous reconstruction technique for tomographic particle image velocimetry, Experiments in Fluids 47 (2009) 553.

[51] R. Gordon, A tutorial on ART (algebraic reconstruction techniques), IEEE Transactions on Nuclear Science 21 (1974) 78-93.

[52] Y. Zhao, X. Li, L. Ma, Multidimensional Monte Carlo Model for Two-photon Laser-induced Fluorescence and Amplified Spontaneous Emission, Computer Physics Communications 183 (2012) 1588-1595.

[53] M. Kang, X. Li, L. Ma, Three-dimensional flame measurements using fiber-based endoscopes, Proceedings of the Combustion Institute 35 (2015) 3821-3828.

[54] J. Chen, B. Karim, A.S. Robert. Calibration for high-definition camera rigs with marker chessboard. In: Proc. IEEE Computer Society Conference on Computer Vision and Pattern Recognition Workshops (CVPRW) 2012; 2012: IEEE. p. 29-36.

[55] Z. Zhang, A flexible new technique for camera calibration, IEEE Trans. Pattern Analysis and Machine Intelligence 22 (2000) 1330-1334.

[56] M. Raffel, C.E. Willert, F. Scarano, C.J. Kähler, S.T. Wereley, J. Kompenhans, Particle image velocimetry: a practical guide, Springer2018.

[57] C. Brücker, 3D scanning PIV applied to an air flow in a motored engine using digital high-speed video, Measurement Science and Technology 8 (1997) 1480.

[58] M. Xu, S. Li, Y. Wu, L. Jia, Q. Lu, Effects of CO2 on the fuel nitrogen conversion during coal rapid pyrolysis, Fuel 184 (2016) 430-439.

[59] J. Soria, C. Atkinson, Towards 3C-3D digital holographic fluid velocity vector field measurement—tomographic digital holographic PIV (Tomo-HPIV), Measurement science and technology 19 (2008) 074002.

[60] C. Atkinson, S. Coudert, J.-M. Foucaut, M. Stanislas, J. Soria, The accuracy of tomographic particle image velocimetry for measurements of a turbulent boundary layer, Experiments in Fluids 50 (2011) 1031-1056.

[61] H.-Y. Zhu, C.-Y. Wang, H.-P. Wang, J.-J. Wang, Tomographic PIV investigation on 3D wake structures for flow over a wall-mounted short cylinder, Journal of Fluid Mechanics 831 (2017) 743-778.

[62] G.E. Elsinga, Tomographic particle image velocimetry and its application to turbulent boundary layers, Delft University of Technology, 2008.

[63] G. Elsinga, B. Van Oudheusden, F. Scarano. Experimental assessment of tomographic-PIV accuracy. In: 13th International Symposium on Applications of Laser Techniques to Fluid Mechanics; 2006; Lisbon, Portugal. p. 1-11.

[64] N. Liu, L. Ma, Hybrid diagnostic for optimizing domain size and resolution of 3D measurements, Optics letters 43 (2018) 3842-3845.

[65] Y. Wu, W. Xu, L. Ma, Kilohertz VLIF (volumetric laser induced fluorescence) measurements in a seeded free gas-phase jet in the transitionally turbulent flow regime, Optics and Lasers in Engineering 102 (2018) 52-58.

[66] Q. Lei, Y. Wu, H. Xiao, L. Ma, Analysis of four-dimensional Mie imaging using fiber-based endoscopes, Applied Optics 53 (2014) 6389-6398.

[67] W. Cai, L. Ma, Comparison of Approaches Based on Optimization and Algebraic Iteration for Binary Tomography, Computer Physics Communications 181 (2010) 1974-1981.

[68] W. Cai, X. Li, L. Ma, Practical aspects of implementing three-dimensional tomography inversion for volumetric flame imaging, Applied Optics 52 (2013) 8106-8116.

[69] P.C. Hansen, Analysis of discrete ill-posed problems by means of the L-curve, SIAM review 34 (1992) 561-580.

[70] E. Aarts, J. Korst, Simulated annealing and Boltzmann machines, Wiley1989.

[71] W. Cai, D.J. Ewing, L. Ma, Investigation of temperature parallel simulated annealing for optimizing continuous functions with application to hyperspectral tomography, Applied Mathematics and Computation 217 (2011) 5754-5767.

[72] Q. Lei, Y. Wu, W. Xu, L. Ma, Development and validation of a reconstruction algorithm for three-dimensional nonlinear tomography problems, Optics express 24 (2016) 15912-15926.

[73] M.W. Kang, X. Li, L. Ma. Calibration of fiber bundles for flow and combustion measurements. In: 52nd Aerospace Sciences Meeting; 2014. p. 0397.

[74] J.Y. Bouguet, Complete camera calibration toolbox for Matlab. http://www.vision.caltech.edu/bouguetj/calib_doc/index.html.

[75] M. Kang, Y. Wu, L. Ma, Fiber-Based Endoscopes for 3D Combustion Measurements:View Registration and Spatial Resolution, Combustion and Flame 161 (2014) 3063–3072.

[76] M. Stark, Optical Flow PIV: Improving the Accuracy and Applicability of Particle Image Velocimetry, ETH Zürich, 2013.

[77] D.J. Acheson, Elementary fluid dynamics, Oxford University Press1990.

[78] U. Tiede, K.H. Höhne, M. Bomans, A. Pommert, M. Riemer, G. Wiebecke, Investigation of medical 3D-rendering algorithms, IEEE computer graphics and applications 10 (1990) 41-53.

[79] R. Banasiak, M. Soleimani, Shape based reconstruction of experimental data in 3D electrical capacitance tomography, NDT & E International 43 (2010) 241-249.

[80] B.R. Halls, D.J. Thul, D. Michaelis, S. Roy, T.R. Meyer, J.R. Gord, Single-shot, volumetrically illuminated, three-dimensional, tomographic laser-induced-fluorescence imaging in a gaseous free jet, Optics express 24 (2016) 10040-10049.

[81] B.R. Halls, P.S. Hsu, N. Jiang, E.S. Legge, J.J. Felver, M.N. Slipchenko, S. Roy, T.R. Meyer, J.R. Gord, kHz-rate four-dimensional fluorescence tomography using an ultraviolet-tunable narrowband burst-mode optical parametric oscillator, Optica 4 (2017) 897-902.

[82] J. Floyd, A. Kempf, Computed tomography of chemiluminescence (CTC): high resolution and instantaneous 3-D measurements of a matrix burner, Proceedings of the Combustion Institute 33 (2011) 751-758.

[83] L. Ma, Q. Lei, J. Ikeda, W. Xu, Y. Wu, C.D. Carter, Single-shot 3D flame diagnostic based on volumetric laser induced fluorescence (VLIF), Proceedings of the Combustion Institute 36 (2017) 4575-4583.

[84] L. Ma, Q. Lei, Y. Wu, W. Xu, T.M. Ombrello, C.D. Carter, From ignition to stable combustion in a cavity flameholder studied via 3D tomographic chemiluminescence at 20 kHz, Combustion and Flame 165 (2016) 1-10.

[85] B.R. Halls, P.S. Hsu, S. Roy, T.R. Meyer, J.R. Gord, Two-color volumetric laser-induced fluorescence for OH and temperature in turbulent reacting flows, Optics letters 43 (2018) 2961-2964.

[86] B.R. Halls, N. Jiang, T.R. Meyer, S. Roy, M.N. Slipchenko, J.R. Gord, 4D spatiotemporal evolution of combustion intermediates in turbulent flames using burst-mode volumetric laser-induced fluorescence, Optics letters 42 (2017) 2830-2833.

[87] L. Ma, Q. Lei, T. Capil, S.D. Hammack, C.D. Carter, Direct comparison of two-dimensional and three-dimensional laser-induced fluorescence measurements on highly turbulent flames, Optics letters 42 (2017) 267-270.

[88] B.R. Halls, J.R. Gord, T.R. Meyer, D.J. Thul, M. Slipchenko, S. Roy, 20-kHz-rate three-dimensional tomographic imaging of the concentration field in a turbulent jet, Proceedings of the Combustion Institute 36 (2017) 4611-4618.

[89] H. Wang, L. Ma, Thermal management of a large prismatic battery pack based on reciprocating flow and active control, International Journal of Heat and Mass Transfer 115 (2017) 296-303.

[90] L. Ma, Nonintrusive and multidimensional optical diagnostics and their applications in the study of thermal-fluid systems, Heat Transfer Engineering 37 (2016) 359-368.

[91] M. Kang, Y. Wu, L. Ma, Fiber-Based Endoscopes for 3D Combustion Measurements:View Registration and Spatial Resolution, Combustion and Flame 16 (2014) 3063–3072.

[92] J. Floyd, P. Geipel, A.M. Kempf, Computed Tomography of Chemiluminescence (CTC): Instantaneous 3D measurements and Phantom studies of a turbulent opposed jet flame, Combustion and Flame 158 (2011) 376-391.

[93] X. Li, L. Ma, Capabilities and limitations of 3D flame measurements based on computed tomography of chemiluminescence, Combust. Flame 162 (2015) 642–651.

[94] L. Ma, Y. Wu, Q. Lei, W. Xu, C.D. Carter, 3D flame topography and curvature measurements at 5 kHz on a premixed turbulent Bunsen flame, Combustion and Flame 166 (2016) 66-75.

[95] B.R. Halls, J.R. Gord, N. Jiang, M. Splichenko, S. Roy, T.R. Meyer. High-speed three-dimensional tomographic measurements for combustion systems. In: 32nd AIAA Aerodynamic Measurement Technology and Ground Testing Conference; 2016. p. 4027.

[96] Y. Wu, W. Xu, Q. Lei, L. Ma, Single-shot volumetric laser induced fluorescence (VLIF) measurements in turbulent flows seeded with iodine, Optics Express 23 (2015) 33408-33418.

[97] J.-Y. Bouguet, Camera calibration toolbox for matlab, (2004).

[98] K. Strobl, W. Sepp, S. Fuchs, C. Paredes, K. Arbter, Camera calibration toolbox for Matlab, Pasadena, CA, (2006).

[99] T. Bell, J. Xu, S. Zhang, Method for out-of-focus camera calibration, Applied optics 55 (2016) 2346-2352.

[100] B. Li, N. Karpinsky, S. Zhang, Novel calibration method for structured-light system with an out-of-focus projector, Applied optics 53 (2014) 3415-3426.

[101] W. Xu, N. Liu, L. Ma, Super resolution PLIF demonstrated in turbulent jet flows seeded with I 2, Optics & Laser Technology 101 (2018) 216-222.

[102] L. Ma, W. Cai, Determination of the Optimal Regularization Parameters in Hyperspectral Tomography, Applied Optics 47 (2008) 4186.

[103] J. Dai, T. Yu, L. Xu, W. Cai, On the regularization for nonlinear tomographic absorption spectroscopy, Journal of Quantitative Spectroscopy and Radiative Transfer 206 (2018) 233-241.

[104] L. Ma, W. Cai, Numerical Investigation of Hyperspectral Tomography for Simultaneous Temperature and Concentration Imaging, Applied Optics 47 (2008) 3751-3759.

[105] W. Cai, X. Li, F. Li, L. Ma, Numerical and experimental validation of a three-dimensional combustion diagnostic based on tomographic chemiluminescence, Opt. Express 21 (2013) 7050-7064.

[106] C.A. DiMarzio, Optics for Engineers, Crc Press2011.

[107] X. Li, L. Ma, Volumetric imaging of turbulent reactive flows at kHz based on computed tomography, Optics express 22 (2014) 4768-4778.

[108] P.J. Van Laarhoven, E.H. Aarts, Simulated annealing, Simulated annealing: Theory and applications, Springer1987, pp. 7-15.

[109] D. Mishra, J.P. Longtin, R.P. Singh, V. Prasad, Performance evaluation of iterative tomography algorithms for incomplete projection data, Applied optics 43 (2004) 1522-1532.

[110] J.M. Seitzman, G. Kychakoff, R.K. Hanson, Instantaneous temperature field measurements using planar laser-induced fluorescence, Optics letters 10 (1985) 439-441.

[111] A. Lozano, B. Yip, R. Hanson, Acetone: a tracer for concentration measurements in gaseous flows by planar laser-induced fluorescence, Experiments in Fluids 13 (1992) 369-376.